RGNZ/MGPB

Middle-Late Miocene Tidal-related Deposits of the Binio Formation: the Sedimentary and Stratigraphic Records during Inversion of the Central Sumatra Basin, Indonesia

Rudarsko-geološko-naftni zbornik
(The Mining-Geology-Petroleum Engineering Bulletin)
UDC: 551.1; 551.24; 551.8
DOI: 10.17794/rgn.2025.1.10

Original scientific paper

Aurio Erdi[1,4]*, Afrizon Setiawan[2], Ismail Zulmi[2], Alan Rene Inabuy[2],
Rifati Hanifa Az Zahra[2], Eric Edwin[2], Ivan Praja Andhika[3], Dany Auliansyah[3], Edward Wijaya[4]
[1]*Research Centre for Geological Resources, National Research and Innovation Agency (BRIN), Indonesia*
[2]*Energi Mega Persada Bentu Limited (EMP Bentu Ltd)*
[3]*Rock Flow Dynamics*
[4]*PT Kejora Gas Bumi Mandiri*

Abstract

The distribution of tidal-related deposits can be controlled by structural growth. This structural growth can be reflected, for example, by inversion structures in a back-arc basin. An example of such a structure is found in the Central Sumatra Basin (CSB), Indonesia. However, there are limited detailed studies using 3D seismic, well, and core data to understand how structural growth controls sedimentary processes and tidal deposit distributions in the CSB. This study utilizes these data to investigate the sedimentary processes and distributions of the Middle-Late Miocene Binio Formation, which was deposited during basin inversion. Sedimentological analysis, sequence stratigraphy, and Root Mean Square (RMS) attribute analysis were conducted on these data. Sedimentological analysis of the core data revealed the presence of tidal sand body and open marine facies. Furthermore, by integrating gamma-ray log and laboratory data, parasequences bounded by flooding surfaces were identified. The stratigraphic framework showed that the tidal sand body occurred before and after maximum flooding surfaces, forming transgressive and regressive tidal sand ridges. RMS attribute analysis indicated a consistent NW-trending orientation of these ridges near the flooding surfaces, implying the influence of a NW-trending tidal current, and a NE-trending paleo-shoreline near the Barisan Mountain, which affected sedimentary distribution and paleogeography during the Middle-Late Miocene. Additionally, the investigation of the relationship between ridges and reverse faults revealed that the ridges were likely controlled by tectonic activities. This study highlights that the temporal and spatial evolutions of the ridges in the CSB was driven by the interaction between sediment supplies and accommodation spaces, likely influenced by reverse fault growth and sea-level variations.

Keywords:
Binio formation; tidal sand ridge; basin inversion; Central Sumatra Basin; sequence stratigraphy

1. Introduction

The Central Sumatra Basin (CSB) in Indonesia has undergone complex Neogene tectonic evolutions since the Early Miocene, characterized by rifting and inversion events (e.g. **Heidrick and Aulia, 1993; Yarmanto et al., 1995; Barber et al., 2005**). These inversion events have been recorded in a few formations, including the Middle-Late Miocene Binio Formation (e.g. **De Coster, 1975; Yuwono et al., 2012**) or the Lower Petani Formation (e.g. **Roezin, 1974; Mertosono, 1975**). Geochemical analysis (**Sundararaman and Teerman, 1991**) and a combination of 2D seismic data, regional surface, conventional core (**De Coster, 1974; Mertosono and Nayoan, 1974; Mertosono, 1975**), and/or wireline logs (**Roezin, 1974; Setiawan et al., 2014**) have been used to suggest that the Binio Formation was deposited in marginal or shallow marine environments. Although insight into the regional depositional environment of the CSB were provided by these previous studies, a detailed understanding of sedimentology and/or sequence stratigraphy processes during the Middle-Late Miocene basin inversion was not offered.

Conventional core was used by **Setiawan et al. (2014)** to illustrate a sandstone lithofacies in the Binio Formation, suggesting a tidal ridge in a tidal-dominated settings. Wireline logs and 2D seismic data were also employed to depict distribution of the sandstone lithofacies, resulting into a low-resolution, map-view distribution of the tidal ridges. Although the understanding of facies distribution and depositional settings of the Binio Formation was enhanced by their work, information on the geometry and control of system tracts over the sandstone distribution was limitedly provided. Thus, a full understanding of sedimentary dynamics and sequence stratigraphy processes for the Binio Formation remains lacking.

---

* Corresponding author: Aurio Erdi
e-mail address: auri002@brin.go.id

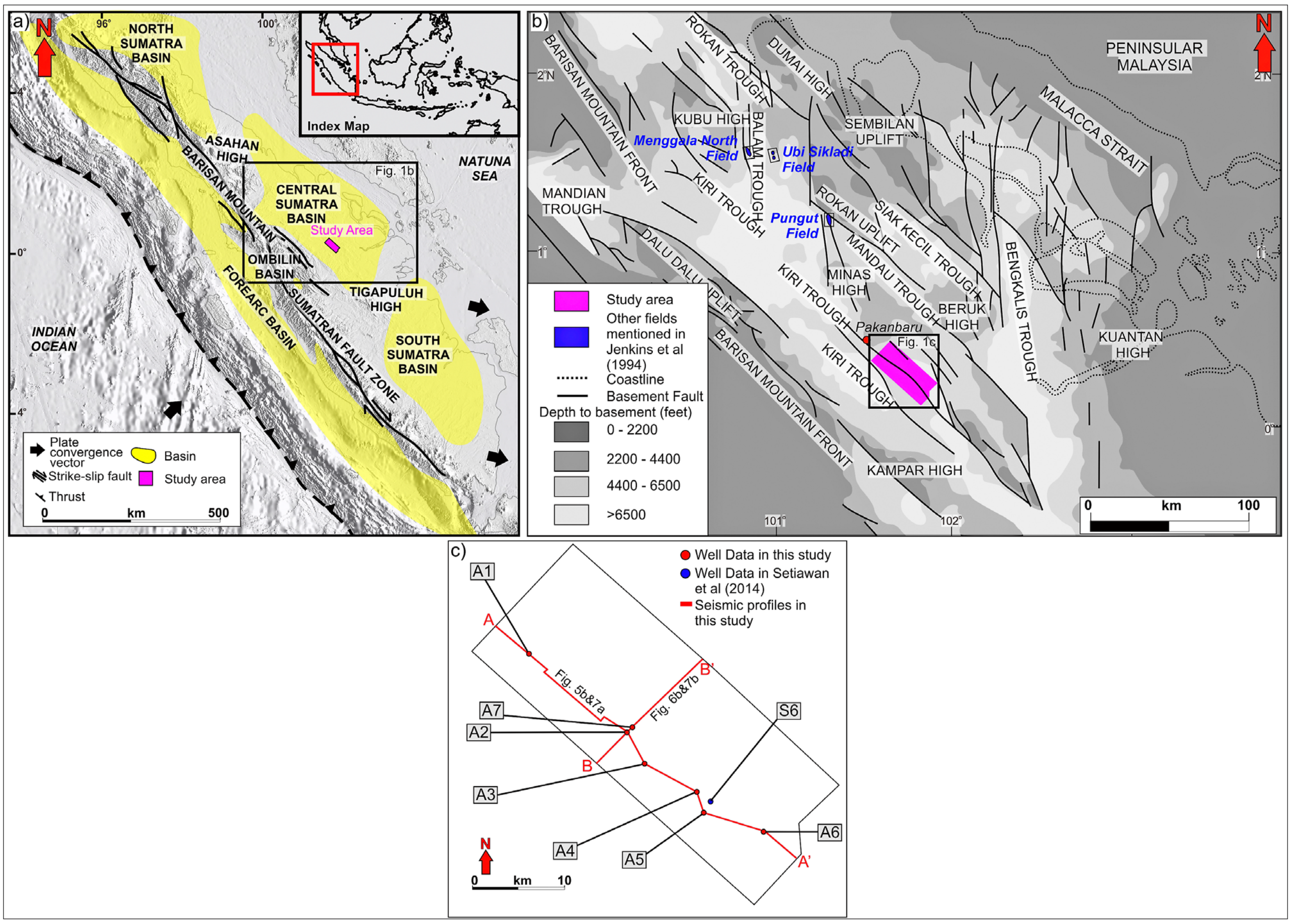

Figure 1: (a) The location of the study area. The base elevation map was derived from **GEBCO (2020)**. (b) The regional structural framework at the basement level of the Central Sumatra Basin. Geological information was compiled from **Heidrick and Aulia (1993)** and **Barber et al. (2005)**. (c) The map showing the relative locations of wells and seismic sections, illustrated in this study (i.e. A1-A7) and in **Setiawan et al (2014**; i.e. S6). The red arrow indicates the North (N) direction.

It has been demonstrated in previous studies that structural growth can significantly influence sedimentary facies and their distributions. For example, facies in the deltaic sediments of the Niger Delta (e.g. **Back et al., 2006**) and basin floor fans in the UK/Norwegian Central Graben (e.g. **Roberts et al., 1990; Cooper and Warren, 2020**) have been shown to be controlled by growth faults, while tidal-related deposits were controlled by the development of thrust sheets in the Pyrenees (**Martinius, 2012**). Despite this knowledge being well-established, no publication has yet addressed the impact of fault growth on sedimentary distributions within the back-arc basin of Sumatra. Specifically, the influence of reverse faults on the distribution of the Binio Formation during the Miocene-Recent basin inversion remains unexamined.

This paper focuses on the area located in the southeastern part of the Kiri Trough in the CSB, Indonesia (see **Figure 1b**). The trough, which trends NW, was formed as an extensional graben during the earliest phase of the structural development of the CSB (**Barber et al., 2005**). A relatively recent study has shown that the trough contains the Middle-Late Miocene Binio Formation, deposited in a tidal-dominated environment during basin inversion (e.g. **Setiawan et al., 2014**). Wireline logs, conventional core, and high-quality 3D seismic reflection data from the southeastern part of the Kiri Trough, CSB, Indonesia are used in this paper (see **Figure 1b**). Through these data in this area, the following questions are addressed: (i) How are the variations and distributions of vertical and lateral facies and the sedimentary processes of tidal-dominated deposits in the Binio Formation related? and (ii) What is the impact of basin inversion on the paleogeography of this formation in the CSB? Sedimentological processes and sequence stratigraphy framework of this formation and their relation to the Middle-Late Miocene basin inversion are discussed, thereby enhancing the understanding of the tectonostratigraphic evolution of the CSB.

2. Geological settings

The study area is located in the CSB, Indonesia (see **Figure 1a**). This basin, one of the inverted back-arc rift

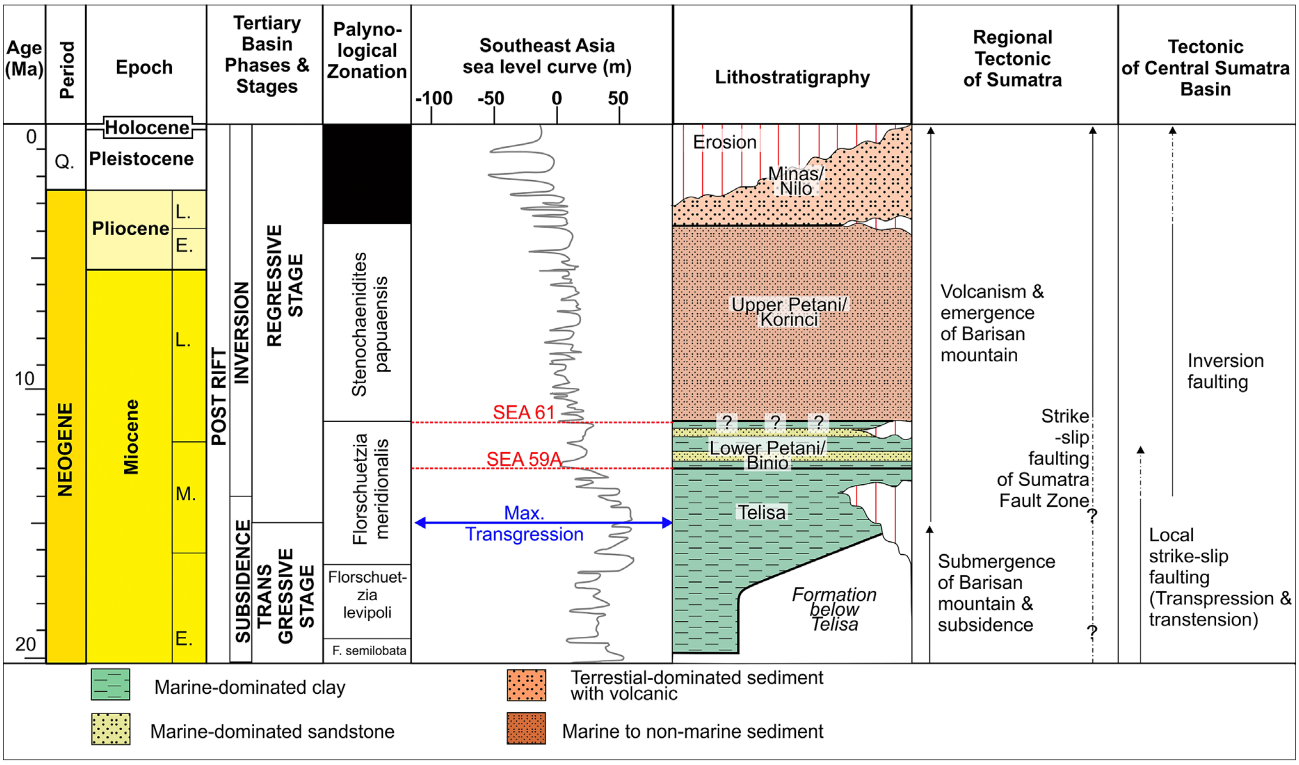

Figure 2: The tectonostratigraphy of the Central Sumatra Basin. Age, basin phases, lithostratigraphy, and regional tectonics of Sumatra and the Central Sumatra Basin were compiled from **De Coster (1975)**, **Heidrick and Aulia (1993)**, and **Barber et al. (2005)**. The age of the Binio Formation was defined by **Geoservices (2019)** in the study area using biostratigraphy data, following the palynological zonation of **Ramli (1988).** The age of the Binio Formation was consistent with the sea-level curve, depositional cycle, and/or sequence biostratigraphy framework for Southeast Asia from **Morley et al. (2021)** between SEA59A-SEA61.

basins, is currently positioned behind the active subduction zone of Sumatra and along the leading edge of Sundaland (e.g. **Heidrick and Aulia, 1993; William and Eubank, 1995; Barber et al., 2005**). The CSB spans nearly 300 km in width, bounded by the Malacca Strait to the northeast and the Barisan Mountains to the southwest (see **Figure 1**). To the northwest and southeast, the basin is constrained by the Asahan and Tigapuluh highs, respectively, extending across Sumatra from 2°N to 1°S (**Barber et al., 2005**).

Three main stages of lithospheric deformation have been experienced by the CSB since the Paleogene. The first stage was marked by rifting during the Eocene (45 Ma) (**Heidrick and Aulia, 1993; Yarmanto et al., 1995; Barber et al., 2005**), being related to crustal attenuation due to the subduction of the Indian Ocean Plate with Sundaland (e.g. **Eubank and Makki, 1981; William and Eubank, 1995**). This basin opening was accommodated by present-day NNW–SSE and N–S lineaments in the basement, indicating highs and troughs that reflect the presence of horst and graben structures across the CSB (**Heidrick and Aulia, 1993; Barber et al., 2005**) (see **Figure 1b**). The second stage was represented by a post-rift subsidence phase, associated with strike-slip faulting that has been active since the Early Miocene (28 Ma) (e.g. **De Coster, 1975; Heidrick and Aulia, 1993; Yarmanto et al., 1995**; **Figure 2**). This strike-slip faulting was recorded by the nucleation of NNE–SSW transtensional wrenching and the reactivation of N–S faults as dextral wrench faults (e.g. **Heidrick and Aulia, 1993; Barber et al., 2005**). The third stage was characterized by positive tectonic inversion and reverse faulting from the Middle Miocene (13 Ma) to the present (e.g. **Eubank and Makki, 1981; Heidrick and Aulia, 1993; Setiawan et al., 2014**; **Figure 2**). This inversion was driven by NNE–SSW compression that was related to the onset of NNE subduction along the NW-trending of Sumatra margin (e.g. **Heidrick and Aulia, 1993; Figure 1a**), inducing the reactivation of NNE–SSW wrench faults as WSW-directed thrust faults (e.g. **Yarmanto et al., 1995; Barber et al., 2005**). The inversion was also associated with the uplift of the proto-Barisan Mountains and simultaneous subsidence along the axis of the back-arc basin (e.g. **Yarmanto et al., 1995; Barber et al., 2005**), consistent with the dextral motion of the Sumatra Fault Zone since 11 Ma (e.g. **Ginger et al., 1993; Pubellier and Morley, 2014**).

During the Early Miocene subsidence phase, rich-foraminifera, grey-brown shales (**e.g. Roezin, 1974; Mertosono, 1975; William and Eubank, 1995**), interbedded with limestone and fine-grained glauconitic sandstones (e.g. **De Coster, 1975; Lee, 1982**) were deposited.

These sedimentary units were defined as the Telisa Formation, deposited in shallow (**Roezin, 1974; Mertosono, 1975; Barber et al., 2005**) or oxic-suboxic marine environments (**Sundararaman and Teerman, 1991**). The Telisa Formation spans environments ranging from inner littoral to outer sublittoral, with deeper marine conditions prevailing to the south (**Lee, 1982; Heidrick and Aulia, 1993**). Maximum marine transgression, which peaked at 15.5-13 Ma, marked the deposition of the Telisa Formation in the CSB (**De Coster, 1975; William and Eubank, 1995; Morley et al., 2021; Figure 2**). Sedimentary deposition during this time was marked by reduced sedimentary input from the Barisan Mountains due to regional transgression outpacing mountain uplift and basin subsidence in the back-arc basins (**Barber et al., 2005**). During this period, the source areas in the Malayan Shield were significantly reduced in size and relief, with the Barisan Mountains nearly submerged (**Barber et al., 2005**).

Since the Middle Miocene (13 Ma) at the end of SEA59A (e.g. **Mertosono and Nayoan, 1974; Lee, 1982; Morley et al., 2021; Figure 2**), grey to brownish-grey fossiliferous, silty, glauconitic shale, and interbeds of 0.5-9 m thick sand was deposited (e.g. **Roezin, 1974; De Coster, 1975; Mertosono, 1975; Lee, 1982; Sundararaman and Teerman, 1991; Jenkins et al., 1994**). These sedimentary units were defined as the Binior or Lower Petani Formation (e.g. **Mertosono and Nayoan, 1974; De Coster, 1975; Lee, 1982**). Furthermore, the first downhole occurrence (FDO) of *Florschuetzia trilobata* at 335 m recorded at the top of the Binio Formation (**Geoservices, 2019**), suggesting a palynological zonation of *Florschuetzia meridionalis* that reflects 11.3 Ma (**Ramli, 1988; Yakzan et al., 1996**) or SEA61 (**Morley et al., 2021; Figures 1**). Sandstones in this formation are characterized by sedimentary structures of parallel, cross, and wavy, flaser, lenticular, and herringbone cross-lamination with lateral distribution of up to c. 35 km (**Setiawan et al., 2014**). These sandstone units change upward into clay shales and decrease in foraminifera abundance upward (e.g. **Mertosono and Nayoan, 1974**), reflecting a progressively shallowing environment (**Lee, 1982; Heidrick and Aulia, 1993**). The Binio Formation was deposited in oxic-suboxic (**Sundararaman and Teerman, 1991**), marginal (**Mertosono and Nayoan, 1974; Mertosono, 1975**), or very shallow to middle neritic (**Roezin, 1974**), shallow marine (**De Coster, 1975; Morley et al., 2016**), or a tidal-dominated environment (**Setiawan et al., 2014**). Previous studies define the sandstone unit of this formation as either a marine bar in a prograding delta (**Jenkins et al., 1994**) or a tidal ridge in a tidal-dominated setting (**Setiawan et al., 2014**). The sedimentary deposition in Middle Miocene occurred during the early stage of the regressive phase of the CSB (e.g. **De Coster, 1975; Mertosono, 1975; Wongsosantiko, 1976**; **Figure 2**), increasing erosion from the Barisan Mountain range (**Morley et al., 2016**), and a shift in sedimentary provenance from the Peninsular Malaysia solely to the proto-Barisan Mountains (**Eubank and Makki, 1981; Yarmanto et al., 1995**; **Barber et al., 2005**). These interplays of tectonic and sedimentation coincided with a basin inversion from at least 13 Ma (e.g. **Heidrick and Aulia, 1993; Yarmanto et al., 1995**) and dextral motion of the Sumatra Fault Zone (SFZ) since 11 Ma (**Ginger et al., 1993; Pubellier and Morley, 2014**; **Figure 2**).

Although no age-dating records have been defined, during approximately the Late Miocene-Pliocene, when inversion continued to occur, greenish-gray shale that becomes sandier upward (**Roezin, 1974**), with occurrences of coal (**De Coster, 1975**) and/or conglomerate was deposited (**William and Eubank, 1995**). These sedimentary units have been defined as the Korinci (**De Coster, 1975**) or Upper Petani Formation (e.g. **Mertosono and Nayoan, 1974; Heidrick and Aulia, 1993; William and Eubank, 1995**; **Figure 2**), being deposited in environment transitioning from brackish to shallow marine at the base, to paludal, delta plain, and non-marine environments upward (**Barber et al., 2005**).

The inversion still continued during the Pleistocene-Recent times, coeval with the deposition of terrestrial deposits, including alluvial coarse sandstone and gravel (**Mertosono, 1975; Heidrick and Aulia, 1993**), tuffaceous sands and thin coal lenses (**De Coster, 1975**), and/or locally glauconitic sands and clays (**Lee, 1982**). These sedimentary units were defined as the Nilo (**De Coster, 1975**) or Minas Formation (e.g. **Mertosono, 1975; Lee, 1982; Heidrick and Aulia, 1993**), being unconformably overlaid the Upper Petani Formation (**Wongsosantiko, 1976; Figure 2**). The Nilo Formation was deposited during a period of significant uplift along the basin margins at the end of the Pliocene (e.g. **Lee, 1982; Heidrick and Aulia, 1993; Barber et al., 2005**), with their provenance likely originating from the uplifted Barisan Mountains (**De Coster, 1975**).

3. Methods

Conventional core data from a well (A3) and wireline-log data of gamma ray (GR), sonic (DT), density (RHOB), and neutron (NPHI) logs from seven wells (i.e. A1-A7) were used in this study (see **Figure 1c**). The core data from the A3 was recorded up to 8 m of the Binio Formation (see **Figure 3**). Sedimentological analysis was conducted on this core data, documenting grain size, sorting, color variations, sedimentary structures, bed thickness, nature of bounding contacts, and macro-fauna types. This analysis was supported by biostratigraphic data from two wells (i.e. A2-A3), made in previous studies by **Geoservices (2019)**. The wireline log data, however, was recorded up to 470 m of the Binio Formation (see **Figures 4, 5a,** and **6a**). Following **Kieft et al. (2010)**, wireline-log characteristics and cross-plot analyses of DT vs. GR and RHOB vs. NPHI were utilized to identify distinctive wire-

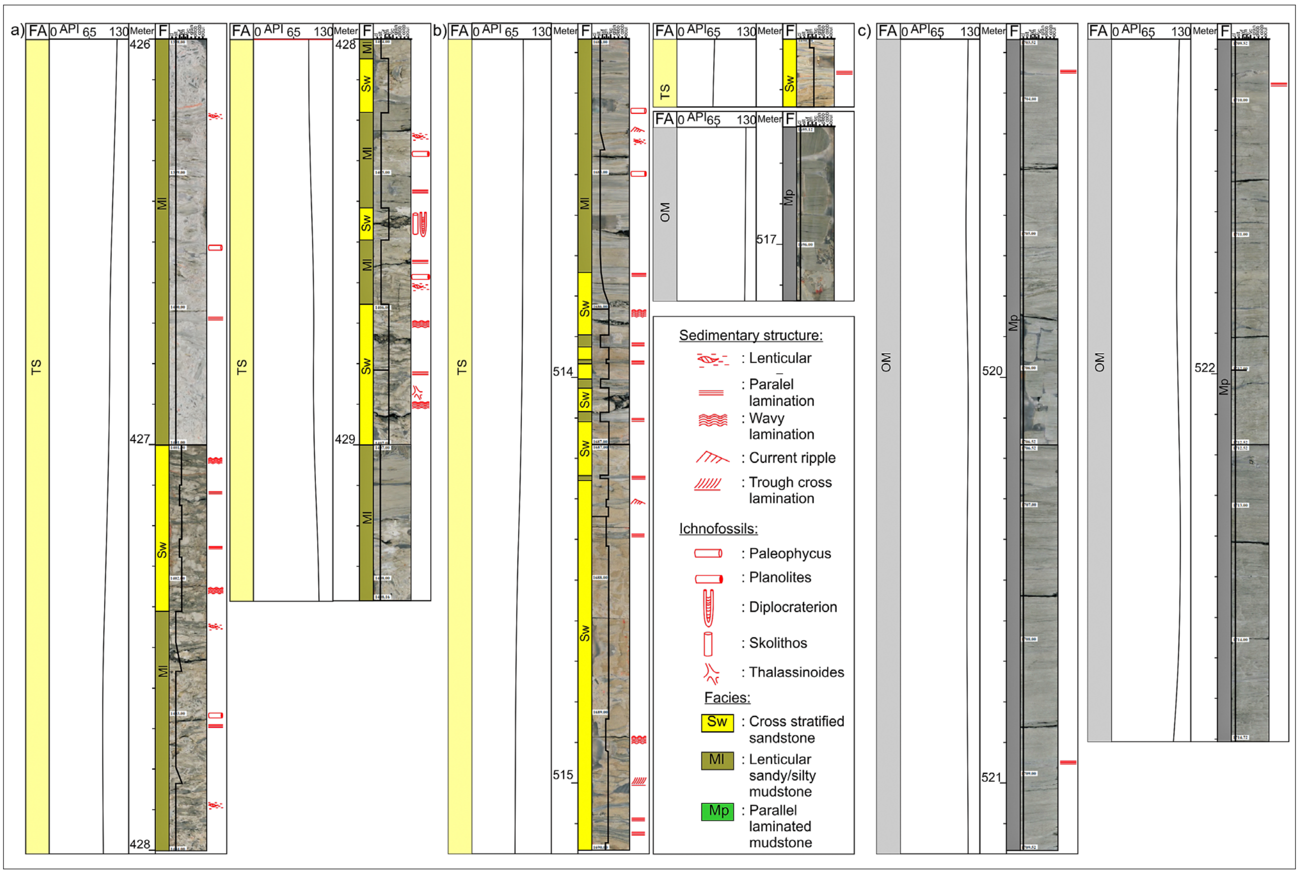

Figure 3: A chart illustrating the conventional core description and photographs, along with GR log characteristics in well A3 (see the location of A3 in **Figure 1c**; also see **supplementary materials** for a larger version of the chart). The facies (F) and facies associations (FA) of the Binio Formation are illustrated, consisting of tidal sand bodies (TS) and open marine (OM) facies (see Table 1 for descriptions). The GR log is presented using the common radioactive unit of the American Petroleum Institute (API).

line-log responses for each facies identified in the core and to qualitatively interpret non-cored intervals within the studied wells (see **Figure 4**).

Sequence stratigraphic correlations across the wells were conducted to illustrate the distribution of facies associations within the study area. The methodology of **Kieft et al (2010)** was followed, using: (i) a descriptive approach of sequence stratigraphy scheme that avoids assumptions of cyclical relative sea-level changes on a sub-regional scale; and, (ii) identification of sequence stratigraphic surfaces of various types and lateral extents without imposing systems-tract frameworks on the stratigraphic packages. Therefore, only maximum flooding surfaces (MFS; e.g. **Posamentier et al., 1988; Galloway, 1989**) and flooding surfaces (FS; e.g. **Van Wagoner et al., 1990; Catuneanu et al., 2011**) were applied without defining system tracts. The MFS was identified through low GR values that may indicate mud-rich intervals, and/or the occurrence of siderite in XRD analysis of **Geoservices (2019)** (**Figure 5a and 6a**; e.g. **Posamentier and Allen, 1999; Catuneanu, 2006**). The FS, however, was defined by an abrupt change from a low GR log value to a high GR log value, which indicate abrupt deepening across a flooding surface (sensu **Van Wagoner et al., 1990**).

A post-stack time migration (PSTM) 2D and 3D seismic dataset covering approximately 430 km² of the Kiri Trough in the CSB was utilized in this study (see **Figure 1b-c**). The dataset images the subsurface to a depth of 3.5 seconds, with a vertical sampling rate of 2 ms. Vertical resolutions in the interval of interest (i.e. Binio Formation) is approximately 30 meters (λ = 120 m) at 0.3 seconds and about 40 meters (λ = 160 m) at 1 seconds below the surface. The dataset includes a line spacing of 12.5 meters for crosslines and 25 meters for inlines, with the inlines and crosslines trending broadly perpendicular and parallel to the predominant southeastward movement of Sundaland-Indian Ocean plate (e.g. **Barber et al., 2005**; **Figure 1a**). The data are presented following SEG conventions, where positive (red) and negative (blue) reflection events represent increases and decreases in acoustic impedance, respectively. A Root Mean Square (RMS) attribute using the seismic dataset was used, given that this attribute is known for its ability to delineate sand bodies (e.g. **Zhuo et al., 2014; Azeem et al., 2016; Ashraf et al., 2019**).

Table 1: A summary of facies and facies associations in the Binio Formation. Thickness reflects the observed thickness from the conventional core. Mineral compositions were obtained from XRD data by **Geoservices (2019)**. The GR log is presented using the common radioactive unit of the American Petroleum Institute (API).

Thickness	Facies Association	Facies	Lithological Description	Mineral composition	Sedimentary structures	Wireline-log character	Interpretation
0.13-1 m	Tidal Sand Body (TS)	Lenticular sandy /silty mudstone (Ml)	Medium to dark brownish grey, well sorted, sandy/silty mudstone.	The mudstone show mainly quartz, K-feldspar, plagioclase, rock fragment (chert, shist and granitic type) and accessory mineral (glaucony, muscovite, zircon, detrital chlorite and calcareous material)	Lenticular of silt-to-very fine sand, current ripple and parallel lamination. Low degree of bioturbation. Burrows include *Planolites* and *Paleophycus*	GR: 43-115 API DT: 397– 682 µ/m NPHI: 0.16 - 0.52 v/v RHOB: 1.8 - 2.27 gcm-3	Ripple and parallel lamination reflect lower flow regime, indicating ripple migration in lateral accretion sets/point bars (c.f. **Boggs, 2014; Plink-Bjorklund, 2005**). Lenticular lamination reflects tidal-influenced deposit, indicating interaction between strong mid-tide currents of incomplete set of ripple and deposition of suspended fines during slack of water (e.g. **Reineck and Singh, 1980; Allen, 1982**).
0.06-1.5 m		Cross stratified sandstone (Sw)	Light yellowish grey, well sorted, very fine-to-fine-grained sandstone. Laminated shale locally present.	The sandstone show mainly quartz, K-feldspar, plagioclase, rock fragment (chert, schist, granitic type), glaucony, detrital chlorite, zircon and carbonaceous material.	Trough cross-lamination, wavy and parallel lamination. Moderate degree of bioturbation. Burrows include *Thalassinoides*, *Skolithos* and *Diplocraterion*.	GR: 53-109 API DT: 512 – 709 µ/m NPHI: 0.079 - 0.52 v/v RHOB: 1.76 - 2.20 gcm-3	Trough cross lamination reflect migration of 2D/3D dunes that was formed by fast flowing tidal currents (**Dalrymple et al., 1990; Olariu et al., 2015**), while wavy likely reflect tidal bundles deposits that was developed in lateral accretion sets/ point bars (c.f. **Shanley et al., 1992; Plink-Bjorklund, 2005**).
up to 3.5 m	Open Marine (OM)	Parallel laminated Mudstone (Mp)	Medium to dark greenish grey, faintly parallel laminated mudstone.	The mudstone generally contain quartz, K-feldspar, plagioclase, and locally contain siderite.	Parallel lamination. Not clear of bioturbation.	GR: 52-136 API DT: 367– 623 µ/m NPHI: 0.31 - 0.64 v/v RHOB: 1.76 - 2.35 gcm-3	Parallel lamination reflects lower flow regime. Muddy character reflects deposition due to suspensions in low energy environment (c.f. **Kieft et al., 2010; Boggs, 2012; Fakhruddin et al., 2023**).

4. Results

The methodology described above has been applied, and the results are presented in this chapter. The results include: 1) Conventional core description and laboratory results; 2) Sequence stratigraphy framework; 3) RMS attribute analysis.

4.1. Core description and laboratory results

Three lithofacies have been identified from conventional cores by classifying distinct characteristics of grain size and sedimentary structures. These facies have been grouped into two facies association, which are described and discussed below, and summarized in **Figure 3** and **Table 1**.

4.1.1. Open marine (OM)

The open marine facies association is represented by a single facies, Mp, in well A3 (see **Figures 1c, 3c** and **5**). The Mp is characterized by mudstones that locally show parallel lamination and a lack of significant bioturbation. XRD analysis of this mudstone has revealed quartz, K-feldspar, and plagioclase, with local occurrences of siderite (**Geoservices, 2019**). Biostratigraphic data, however, shows the presence of calcareous benthics *Cibicides* and a single planktic at 384 mMD along with small arenaceous foraminifera (i.e. *Haplophragmoides, Trochammina, Alveolophragmium, Bathysiphon and Ammobaculites*) at 455 mMD (**Geoservices, 2019**).

The open marine facies association is generally characterized by high GR values across various profiles (see

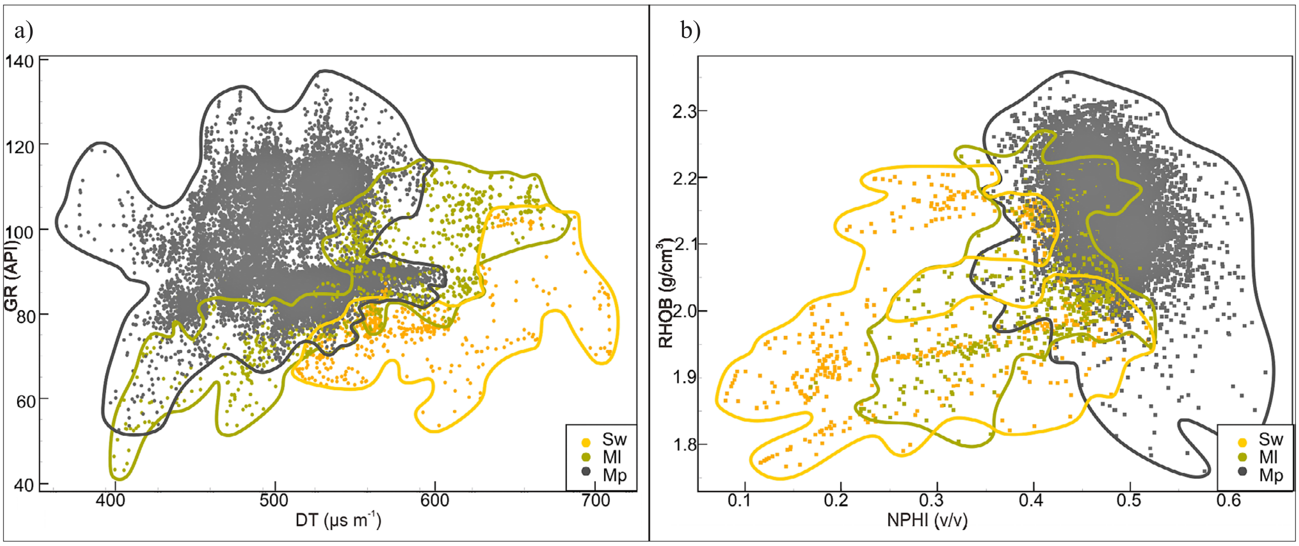

Figure 4: Wireline-log cross-plots of: (a) Gamma Ray (GR) vs. Sonic (DT), and (b) Density (RHOB) vs. Neutron (NPHI). The GR log is presented using the common radioactive unit of the American Petroleum Institute (API). These cross-plots were compiled from seven wells and conventional cores, illustrating the quantitative log characteristics of the Binio Formation facies. Distinctive characteristic of GR vs. DT and RHOB vs. NPHI were identified between the cross-stratified sandstone (Sw) and the lenticular sandy/silty mudstone (Ml). However, significant overlap occurred between the lenticular sandy/silt mudstone (Ml) and the parallel-laminated mudstone (Mp), making it difficult to distinguish these two facies away from core control, indicating shared muddy characteristics between them.

Table 1; Figures 3, 4a, 5a and **6a**). However, in terms of bed-scale variations, this facies is marked by serrated GR-log patterns (see **Figures 3c, 5a** and **6a**). Although the conventional core data do not reveal a distinct contact with other facies, the GR log indicates that this unit either abruptly or gradually overlies deposits of the tidal sand body facies at the base (see **Figures 5a** and **6a**). This contact, where the open marine facies are directly juxtaposed above the tidal sand body, is consistent with a mark of abrupt deepening across a flooding surface of **Van Wagoner et al., (1990)**. As such, the contact is defined as the flooding surface across the well (see **Figures 5a** and **6a**). On the other hand, an abrupt or gradual decrease in GR log value is observed upward to the tidal sand body facies, reflecting an abrupt or gradual contact of open marine with this sand-rich facies at the top. Maximum flooding surfaces (MFS) have been interpreted based on low GR values and/or siderite occurrence identified in XRD of **Geoservices (2019)** (see **Figures 5a** and **6a**). The upward gradual or abrupt decrease in GR log values upward into the tidal sand body facies indicates a corresponding gradual or abrupt shallowing into the sand-rich facies.

4.1.2. Tidal sand body (TS)

The tidal sand body facies association has been identified from up to 90 m of conventional core data, comprising facies Sw and Ml (see **Figure 3**). The base of the tidal sand body is characterized by wavy, parallel, and trough cross-laminated sandstone (facies Sw). Petrographic analysis of this sandstone has revealed quartz, K-feldspar, plagioclase, rock fragments (chert, schist, granitic types), glaucony, detrital chlorite, zircon, and carbonaceous material (see **Table 1**; **Geoservices, 2019**). A moderate degree of bioturbation is observed in the Sw with local traces of *Thalassinoides*, *Skolithos*, and *Diplocraterion* (see **Figure 3**). The Sw facies transitions sharply and gradually into the current ripple and parallel laminated, and lenticular sandy/silty mudstone (facies Ml). Petrographic analysis of this mudstone has revealed primarily quartz, K-feldspar, plagioclase, rock fragments (chert, schist, and granitic types), and accessory minerals (glaucony, muscovite, zircon, detrital chlorite, and carbonaceous material) (see **Table 1**; **Geoservices, 2019**). A low degree of bioturbation in the Ml is shown by the presence of *Planolites* and *Paleophycus* traces (see **Figure 3**).

GR logs show variable profiles on conventional cores through the succession of this facies association. The profiles generally consist of "egg" profiles, characterized by cycles of increasing and decreasing upward trends (see **Figure 3a**). This profile is represented by interbedding between the Ml at the base and top, with the Sw in the center. The egg profiles on the core also display a decreasing upward trend resembling a funnel profile on a larger scale (see **Figure 5a**). In addition, bell profiles, showing an upward increasing trend, are also observed in GR log (see **Figure 3b**). The bell profiles are associated with the Sw at the base, gradually transitioning upward into the Ml. The Sw generally shows relatively lower GR values than the Ml, consistent with its coarser grain size. However, in some intervals, the Sw do not show significantly different GR values compared to the Ml. For example, at 513.8-514.4 mMD, up to 0.15 m of the Sw does not display any different GR values than the Ml (see **Figure 3b**). Despite this, the Ml generally show relatively higher GR values than the Sw, reflecting its muddier characteristics (see **Figure 3b-c**).

Distinctive characteristics of Sw and Ml have been identified from wireline-log cross-plots (see **Figure 4**), and their wireline-log characteristics are summarized in Table 1. The Sw generally shows lower GR values (53-109 API) and NPHI values (0.079 - 0.52 v/v), along with higher DT values (512 – 709 µ/m) and RHOB values (1.76 - 2.20 g/cm^3), relative to other facies. This allows the distribution of Sw to be identified away from the core control. However, Ml is harder to distinguish away from the core control due to significant overlaps with Mp in the wireline-log cross-plots (see **Figure 4** and **Table 1**). The Ml also shows a narrower range of GR log values (43-115 API) compared to the Mp (52-136 API).

The complete tidal sand body facies association is reflected by decreasing or low GR log values, followed by an abrupt increase in GR log values (see **Figures 5a** and **6a**). This pattern suggests that the sand-rich unit of the tidal sand body facies, showing a coarsening upward trend or a massive structure, is abruptly overlain by the mud-rich unit open marine facies. Thus, the top of this facies marks an abrupt deepening across a flooding surface (sensu **Van Wagoner et al., 1990**). The lower contact of this facies shows either a sharp or gradual transition with the open marine facies.

4.2. Sequence stratigraphy framework

Four main maximum flooding surfaces (MFS1-MFS4) and six flooding surfaces (FS1-FS6), that reflect third-order sequence boundaries (**Embry, 1993; 1995**), have been defined and correlated within the intra-Binio Formation to construct a semi-regional sequence stratigraphic framework. This framework illustrates the distribution of facies associations within the study area and is depicted by two section correlations, which are flattened (datum) on the FS4 (see **Figures 5-6**).

4.2.1. Correlations Along Basin Axis

The studied strata have been subdivided into seven intervals, bounded by six flooding surfaces that can be correlated along the axis of the Kiri Trough (see **Figures 5-6**). Some intervals are divided into upper and lower parts by a maximum flooding surface. The first, lowermost interval (below FS6) is characterized by interbedding of tidal sand bodies and open marine deposits. Although the distribution of the tidal sand bodies is poorly constrained by well log data (A5), a tidal sand body has been laterally connected between wells. These tidal sand bodies have developed in the northwest (A1) and central-southern parts of the study area (A4-6), being separated by massive open marine deposits in the central part of the study area (A2-3; **Figure 5a**). In the southeast (A6), the tidal sand bodies thin upward (down to c. 3 m), while in the northwest and central parts (A1 and A4), they thicken upward (up to c. up to c. 9 m). In the second interval (between FS6 and FS5), an open marine deposit has been developed along the NW-trending axis (see **Figure 5a**). Near FS5, this deposit is followed by a thin (up to c. 4.5 m) tidal sand body that has been laterally connected along the northwest and central parts of the study area (A1-5).

In the lowest third interval (between FS5 and FS4), an open marine deposit overlies the sand body near FS5 and has developed along the NW-trending axis. This marine deposit is followed by local interbedding of thin (c. 1.5 m) tidal sand bodies and open marine deposits in the northwestern-central (A2-4) and southeastern parts (A6) of the study area. Toward and near FS4, these sand bodies have been laterally connected along the NW-trending axis and have thickened upward (up to c. 16.5 m) in the northwest (A1-2). The lowest fourth interval (FS4-FS3) overlays the third interval and is characterized by open marine deposits below MFS4. Above MFS4 and toward FS3, local interbedding of thick (up to c. 6 m) tidal sand bodies and open marine deposits have developed along the northwest and central parts of the study area (A2-4; **Figure 5a**).

The lower part of the fifth interval (FS3-FS2) overlays the fourth interval and is characterized by local interbedding of thick (up to c. 12 m) tidal sand bodies and open marine deposits below MFS3 in the northwest, central, and southeast parts (A1-A2, A4, and A6; **Figure 5a**). Above MFS3 and toward FS2, this interval transitions into an open marine deposit, followed by a NW-trending, laterally connected single tidal sand body in the central-southeast (A3-5), or interbedded tidal sand bodies and open marine deposits in the northwest-central (A1-A2) and southeast areas (A6; **Figure 5a**). The interval between MFS3 and FS2 shows that the tidal sand body thins (from 15 to 3 m) from the northwest (A1) toward the central area (A2-A4), consistent with the thinning of FS3-FS2 (from 104 to 23 m) from the northwest southeastward (c.f. **Figures 5a** and **5b**).

The lower part of the sixth interval (FS2-FS1) overlays the fifth interval and is generally represented by open marine deposits below MFS2 (see **Figure 5a**). However, thick (up to c. 7 m) tidal sand body deposits are locally developed between the open marine deposits and has thinned from the northwest to the southeast (A1-A4). These deposits are overlain by interbedded tidal sand bodies and open marine deposits above MFS2 (see **Figure 5a**). The sand bodies are relatively thin (up to c. 6 m) in the northwest (A1-2) and thicker (up to c. 15 m) in the central and southeastern parts (A3-6) of the study area. Near FS1, the uppermost deposit of a tidal sand body has been connected along the NW-trending axis.

The lower part of the last interval (FS1-Binio) overlays the sixth interval (see **Figure 5**). Below MFS1, the last interval is represented by open marine deposits and

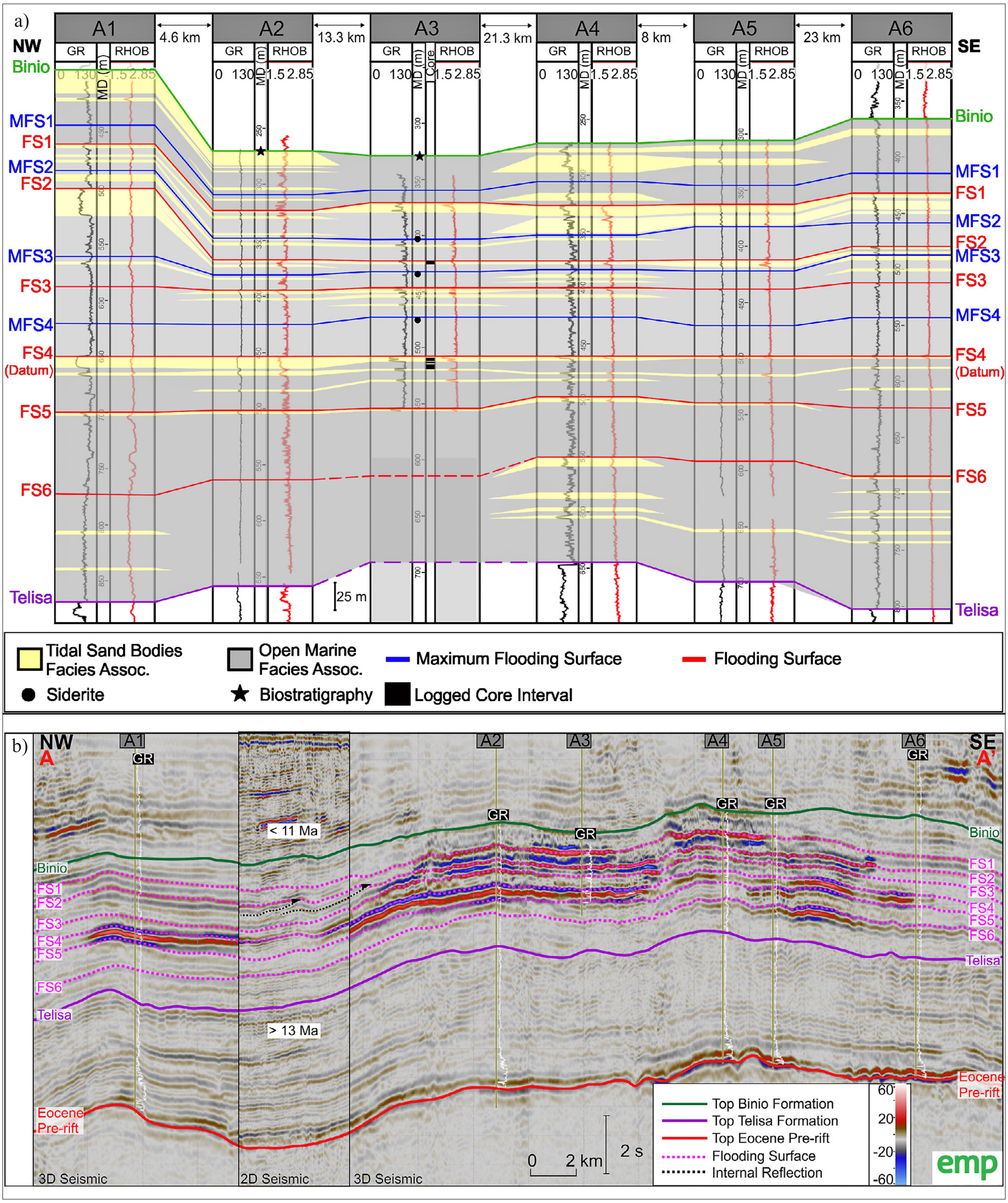

Figure 5: (a) A regional northwest-southeast-oriented well-log correlation. The correlation was constrained by biostratigraphy data from wells A2 and A3 (biostratigraphy samples marked with an asterisk) and seismic stratigraphy thickness. It is subdivided by four maximum flooding surfaces (MFS) and six flooding surfaces (FS) within the intra-Binio Formation. The well-log correlation illustrates the NW-trending distribution of tidal sand bodies, reflecting tidal sand ridges surrounded by open marine facies. This correlation was flattened using FS4 as a datum. (b) A seismic profile along the study area axis (see **Figures 1c** and **8** for the location of the wells and seismic profile). The intra-Binio Formation generally shows conformable and consistent thickness along the strike, but local thickness variations are between FS2 and FS3, with thickening in the northwest and thinning southeastward in both the well correlation and seismic profile. Seismic data courtesy of Energi Mega Persada Bentu Limited.

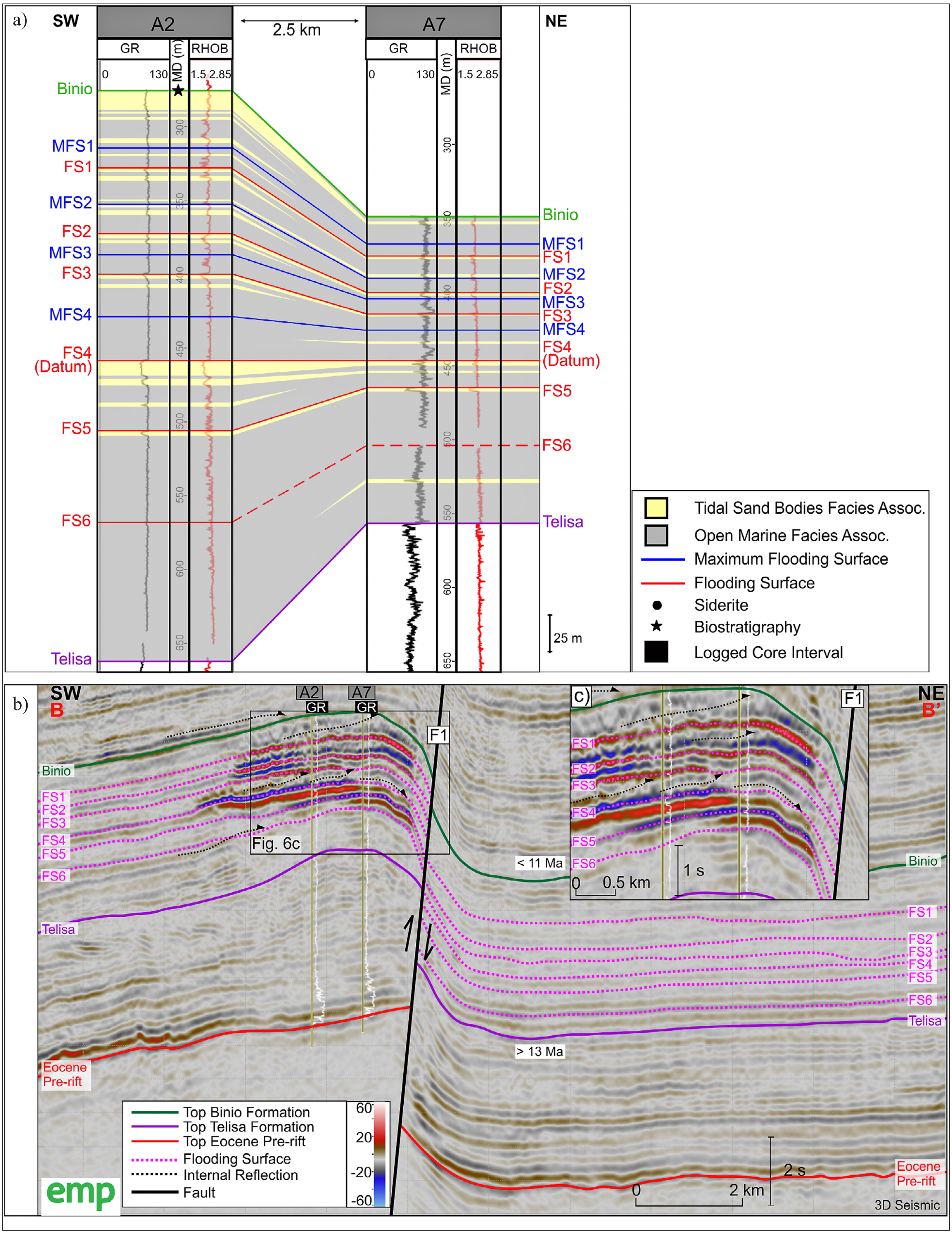

Figure 6: (a) A regional southwest-northeast-oriented well-log correlation. The correlation was constrained by biostratigraphy data from well A2 (biostratigraphy sample marked with an asterisk) and seismic stratigraphy thickness. It is subdivided by four maximum flooding surfaces (MFS) and six flooding surfaces (FS) within the intra-Binio Formation. The well-log correlation illustrates the NE-trending distribution of tidal sand bodies, reflecting tidal sand ridges around open marine facies associations. (b) A seismic profile perpendicular to the study area axis (see **Figures 1c** and **8** for the location of the well and seismic profile). The intra-Binio Formation generally thins toward the northeast, flanking onto the reverse fault (F1). Seismic data courtesy of Energi Mega Persada Bentu Limited.

pp. 123-144, DOI: 10.17794/rgn.2025.1.10

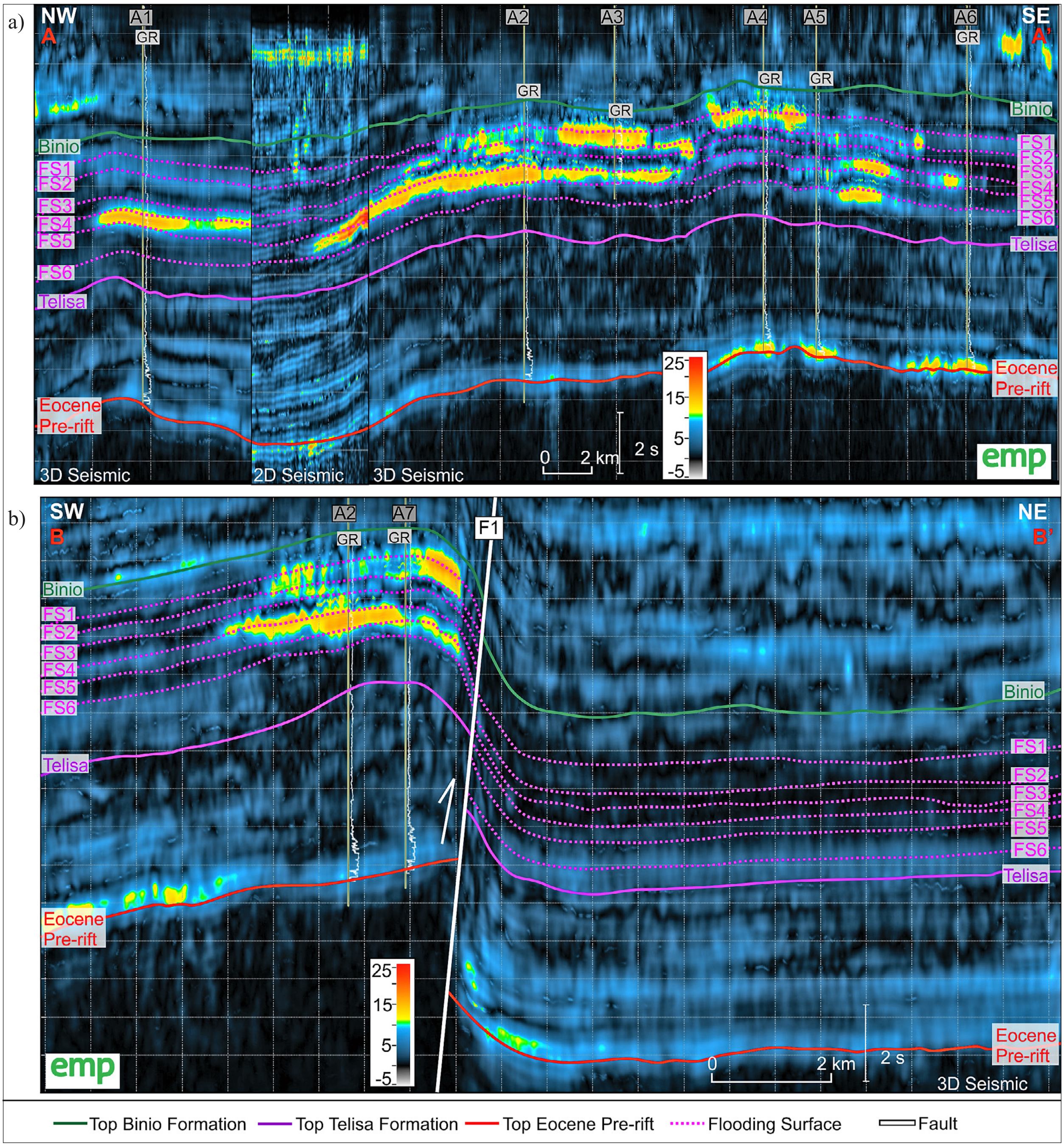

Figure 7: (a) Regional northwest-southeast and (b) southwest-northeast-oriented RMS seismic profiles, showing the distribution of high amplitudes within the intra-Binio Formation. These high amplitudes are consistent with the tidal sand body facies associations observed in well-log correlations in **Figures 5a** and **6a**. See also **Figure 8** for the location of the seismic profiles. Seismic data courtesy of Energi Mega Persada Bentu Limited.

locally thick (up to c. 6 m) tidal sand body deposits in the northwest and southeast (A2 and A4). Above MFS1, the tidal sand bodies thicken upward (up to c. 20 m) in the northwest (A1-2), while local thinning (down to c. 4.8 m) occurs upward in the southeast (A4-5; **Figure 5**).

4.2.2. Correlations perpendicular to basin axis

In the central part of the study area, a thick (up to c. 400 m) succession of seven intervals of the intra-Binio Formation thins northeastward and flanks onto a reverse fault (F1; **Figure 6**). Below FS6, a thin (up to c. 1.5 m) tidal sand body has locally developed near the fold crest (A7; **Figure 6**). Above FS6 and upward to the top of the Binio Formation, the tidal sand bodies generally develop near flooding surfaces (FS1-5), being located near the fold crest (A7; **Figure 6**). These sand bodies have been laterally connected from the southwest to the northeast near the flooding surfaces (FS1-5) and the top of Binio. The tidal sand bodies maintain consistent thickness (up to approximately 3.6 m) near FS1 but thin (down to approximately 2.5 m) near FS2-FS5 and the top of Binio northeastward. This thinning of the sand bodies corresponds with the thinning interval of Binio-FS6 on the southwestern flank of the reverse fault (F1; **Figure 6b**).

4.3. RMS attribute

The lateral distribution of facies association is illustrated by RMS sections and three RMS maps, which show the event of FS1, FS3, and FS4 during the deposition of the Binio Formation (see **Figures 7-8**). RMS sections generally show that the tidal sand bodies in well data correspond to high (>9) amplitude (c.f. **Figures 5, 6** and **7**). For example, a thick (up to 16.5 m) tidal sand body near FS4 is consistent with the high amplitude of RMS at the top of FS4, distributed along a NW-trending axis (c.f. **Figures 5 and 7a**).

The RMS maps show that the distribution of the high amplitudes, associated with the tidal sand bodies at the structural levels of FS1, FS3 and FS4, varies across the study area (see **Figure 8a-c**). These high amplitudes have a NW-trending (N130° E ± 10°) orientation at the structural levels of FS1, FS3, and FS4, and are generally laterally enclosed by low amplitudes. This orientation is consistent with the reverse fault orientation (c. N134°E) in the study area, particularly for high amplitudes in the northwest southward, located along well of A1-A7 (see **Figure 8**). However, the distributions of high amplitudes near flooding surfaces varies in relation to the reverse faults. At the structural levels of FS4 and FS3, high amplitudes are laterally restricted by the reverse faults (see **Figures 7b** and **8a-b**). The distribution of high amplitudes is more extensive at FS4 compared to FS3 (see **Figure 7**, and c.f. **Figures 8a** and **8b**). At the structural level of FS1, however, the distribution of the high amplitudes is more extensive compared to that at structural level of FS3-4, and they also cross the reverse faults (see **Figure 8c**). For example, a high amplitude near well A4 at FS1 extends northeastward.

5. Discussion

The discussion is based on the results described above, which indicate that sedimentology, sedimentary processes and the distribution of facies associations were influenced by changes in sea levels and basin inversions within the Kiri Trough of the CSB during the Middle-Late Miocene.

5.1. Sedimentology of Binio Formation

5.1.1. Sedimentology of open marine facies

The lithology characteristics of this facies association indicate sedimentological process, while biostratigraphy data suggests the depositional environment during deposition of the facies. The fine-grained character of the facies, their parallel laminated character and lack of significant bioturbation suggest deposition from suspension (e.g. **Boggs, 2014; Kieft et al, 2010; Fakhruddin et al., 2023**). This interpretation is supported by biostratigraphic data, showing the presence of calcareous benthics *Cibicides* and a single planktic at 384 mMD, as well as small foraminifera arenaceous (i.e. *Haplophragmoides*, *Trochammina*, *Alveolophragmium*, *Bathysiphon* and *Ammobaculites*) at 455 mMD, which suggest an inner sublittoral marine environment (**Geoservices, 2019**). This inner sublittoral zone reflects a water depth between low tides and down to 100 m below sea level (e.g. **Hedgpeth, 1957**). Based on this biostratigraphic data and the fine-grained lithology, this facies association is interpreted to had been deposited in the open marine area below the low tides level. This interpretation aligns with a facies model for a tide-dominated system, where mud-rich units of open marine deposits may conformably overlay tidal ridges due to sea level changes (**Dalrymple, 2010**).

5.1.2. Sedimentology of tidal sand body facies

The sedimentary processes and depositional environment of the tidal sand body facies are indicated by their lithological characteristics and sedimentary structures. This tidal sand body facies is represented by facies Sw and Ml. Facies Ml shows parallel, ripple lamination and heterolithic lenticular structures, while facies Sw shows trough cross lamination in A3 (see **Figure 3**). In addition, observations of **Setiawan et al. (2014)** on sand-rich units in similar intervals show that the tidal sand body facies consist of parallel, cross, and herringbone lamination, flaser, wavy, and lenticular in S6 (see **Figure 1c**). The herringbone lamination suggests bipolar dip directions of paleoflow (**Dalrymple, 2010**), generated during flood and ebb tides (**Boggs, 2014**). The parallel and ripple laminations reflect episodic deposition by suspension and traction currents in the lower flow regime, respectively (e.g. **Blatt et al., 1980; Boggs, 2014; Figure 3**). Their presence, combined with heterolithic lenticular and wavy structures, indicates tidal deposits influenced by tidal currents that developed in tidal lateral accretion sets (e.g. **Shanley et al., 1992; Plink-Bjorklund, 2005**). The trough cross-lamination, however, suggests the migration of 2D/3D dunes formed by fast-flowing, high-energy tidal currents (**Dalrymple et al., 1990; Olariu et al., 2015**). The vertical succession shows rhythmic interbedding between facies Ml and Sw (see **Figure 3**), implying regular fluctuations in energy regime and suggesting tidal action (e.g. **Dalrymple et al., 1991; Dalrymple, 2010**; **Kieft et al., 2010**). The complexity of tidal and high-energy characteristics suggests that a sand body was deposited in a tidal-dominated setting. This interpretation is consistent with a previous study, indicating that the Binio Formation was deposited in a tidal-dominated setting (**Setiawan et al., 2014**).

GR log data show local vertical variations in the tidal sand body facies. Several intervals of Sw do not show significant difference in GR values compared to Ml, as observed at 513.8-514.4 mMD (see **Figure 3b**). It is speculated that these local observations highlight the limitations of the GR tool, which has a vertical resolution of c. 0.6 m (e.g. **Cannon, 2016**). Furthermore, significant overlaps between Ml and Mp are also observed in the wireline-log cross-plots (see **Figure 4** and **Table 1**). This observation is speculated to reflect the shared muddy characteristics between these two facies within the tidal sand body facies.

5.2. Sedimentary process of the facies associations during basin inversion

Observations from the conventional core, well correlations, and seismic data suggest that the sedimentary processes and dynamics of allogenic or autogenic changes in relative sea-level and/or depositional environments influenced the mud-rich open marine facies associations. Sequence stratigraphy correlations indicate that the distribution of open marine facies was generally controlled by system tract events. During the development of maximum flooding surfaces (between FS and MFS), open marine facies are typically observed, such as between FS4 and MFS4 (see **Figures 5-6**). This observation is interpreted as being related to sediment starvation and/or the entrapment of coarser terrigenous sediment within aggrading fluvial and coastal systems during transgressions, consistent with previous studies (e.g. **Loutit et al., 1988; Galloway, 1989; Catuneanu, 2006**).

The distribution of tidal sand bodies also reflects allogenic or autogenic changes in relative sea-level during the deposition of the Binio Formation and their relationship with system tract events. The sand bodies occur between flooding surfaces and during development (below) or after establishment (above) of the maximum flooding surfaces (see **Figures 5a** and **6a**). They are generally laterally and vertically enclosed by mud-rich open marine facies in well and seismic data (see **Figures 5-8**). Based on these characteristics, combined with their log profile in the GR log, two possible interpretations for the genesis of these tidal sand bodies are proposed: (i) transgressive tidal sand ridges (e.g. **Posamentier, 2002; Lopez et al., 2006**), and/or (ii) regressive sand ridges (e.g. **Berne et al., 1998; Zhang et al., 2017; Longhitano et al., 2021**). These interpretations are supported by: (a) tidal-related sedimentary structures in conventional cores (see **Table 1**); (b) funnel and bell-shaped profiles of tidal sand bodies in the GR log (see **Figure 3**); (c) lateral distribution of high amplitude anomalies representing tidal sand bodies in seismic data (see **Figures 7-8**); and, (d) the distribution of tidal sand bodies during or after the development of MFS (see **Figures 5a** and **6a**). The interpretation of transgressive sand ridges is consistent with a coarsening upward and/or bell-shaped profile of GR or sedimentary log and/or high amplitude anomalies in transgressive system tracts, as illustrated by transgressive tidal shelf ridges in Offshore Northwest Java (e.g. **Posamentier, 2002**) and the East China Sea (e.g. **Berne et al., 2002; Liu et al., 2007**). The interpretation of regressive tidal-influenced sand ridges, however, is consistent with a coarsening upward profile within the falling stage and low-stand system tracts in Southern Italy (**Longhitano et al., 2021**) and high amplitude anomalies in the South China Sea, indicating regressive sand ridges (**Zhang et al., 2017**).

Given the consistency of the data from this study with previous studies above, it is interpreted that the tidal sand bodies in the Middle-Late Miocene Binio Formation reflect transgressive and regressive tidal sand ridges. This interpretation aligns with previous studies that have identified sandstone in the Binio Formation as tidal ridges (**Setiawan et al., 2014**). Two possible mechanisms are proposed to have produced these tidal sand ridges during transgressive system tracts: (a) the erosion of the upper shoreface during sea-level rise, leading to sand-rich deposits in the lower shoreface (e.g. **Bruun, 1962; Dominguez and Wanless, 1992; Catuneanu, 2006**); and (b) tidal reworking of the underlying regressive coastline deposits (e.g. **Posamentier, 2002; Lopez et al., 2016**). It is preferred that the transgressive tidal sand ridges in the study area resulted from a combination of upper shoreface erosion during sea-level rise and tidal reworking. The erosion of the upper shoreface is likely reflected in the disconformity observed in the Binio Formation, located on the edge of the CSB (**De Coster, 1975**). Tidal reworking is indicated by the tidal-related sedimentary structures observed in the conventional core (see **Figure 3**). Regressive tidal sand ridges are suggested to have formed due to cyclical aggradation and progradation during long-term sea-level fall and tectonic uplift (**Longhitano et al., 2021**). It is interpreted that such events also contributed to the deposition of the regressive tidal sand ridges in the study area during the Middle-Late Miocene. This interpretation is consistent with the occurrence of regional regression in the CSB and the uplift of the Barisan Mountain during the deposition of the Middle-Late Miocene Binio Formation (e.g. **Heidrick and Aulia, 1993; Yarmanto et al., 1995; Barber et al., 2005**).

The distribution of tidal sand bodies, as illustrated by high amplitudes in seismic attributes, shows various relationships with the reverse faults. These sand bodies are distributed along a NW-trending orientation at the structural levels of FS4, FS3 and FS1. This orientation aligns with NW-trending high amplitudes observed in the Ubi Sikladi, Menggala North and Pungut Fields, which are located in the CSB (**Figure 1b**; **Jenkins et al., 1994**). Some high amplitudes trending northwest southward in the study area align with the orientation of the reverse faults (see **Figure 8**). These distributions suggest two possible interpretations. First, the NW-trending distribution may reflect the control exerted by reverse faults dur-

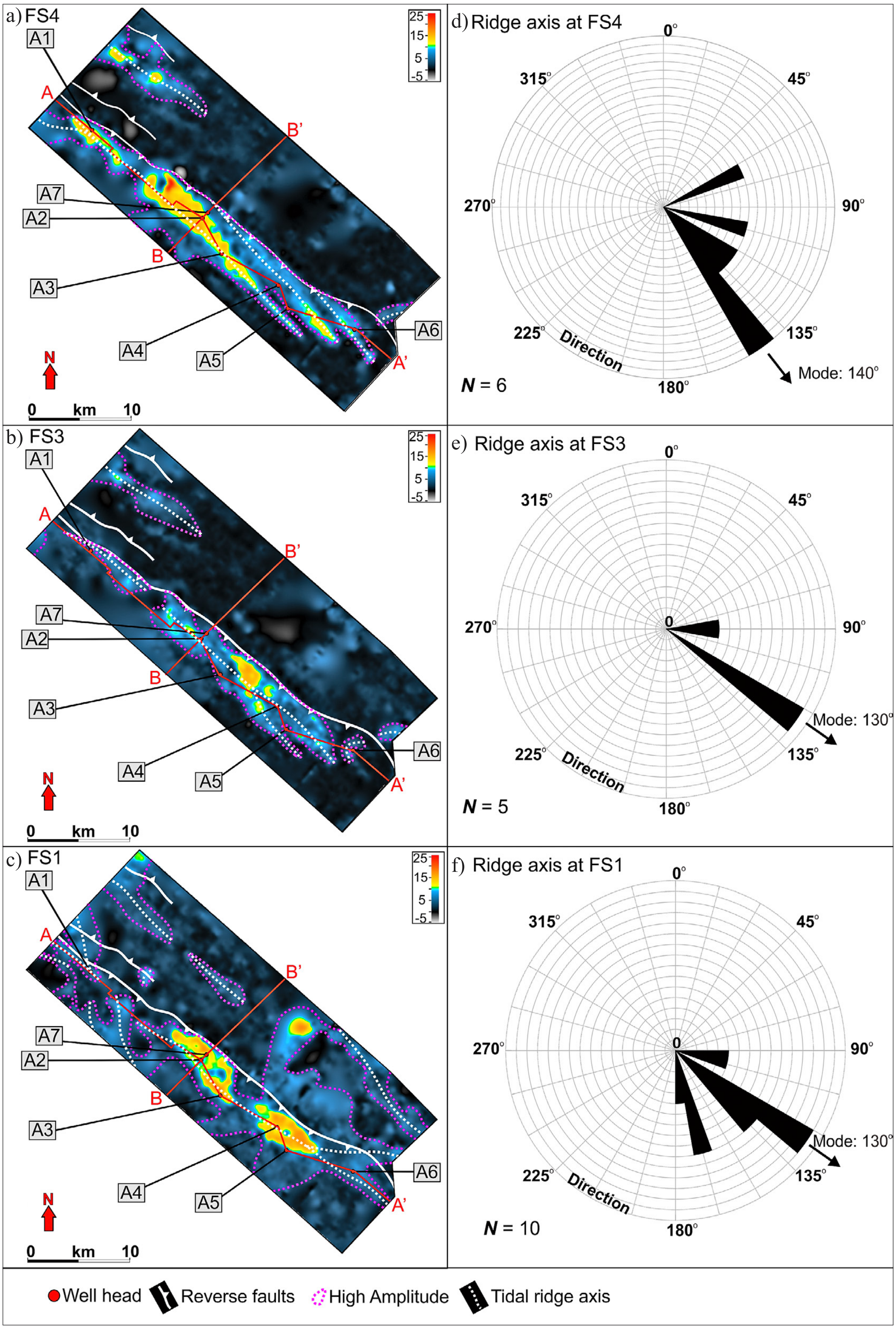

Figure 8: RMS amplitude map at the structural level of the Flooding Surface (FS) for (a) FS4, (b) FS3, and (c) FS1, showing the map-view distributions of high amplitudes that reflect tidal sand body facies associations. At the structural levels of FS4 and FS3, the high amplitudes near reverse faults are laterally restricted by the faults, while at the structural level of FS1, the high amplitudes extend across the fault. Notably, at all structural levels, the distributions of high amplitudes far from faults show a NW-trending orientation. The axes of the high amplitudes are measured, showing dominant orientations of (d) 140° at FS4, (e) 130° at FS3, and (f) 130° at FS1. These orientations indicate the direction of tidal currents during each structural level (see **Figure 9** for reference). The red arrow indicates the North (N) direction.

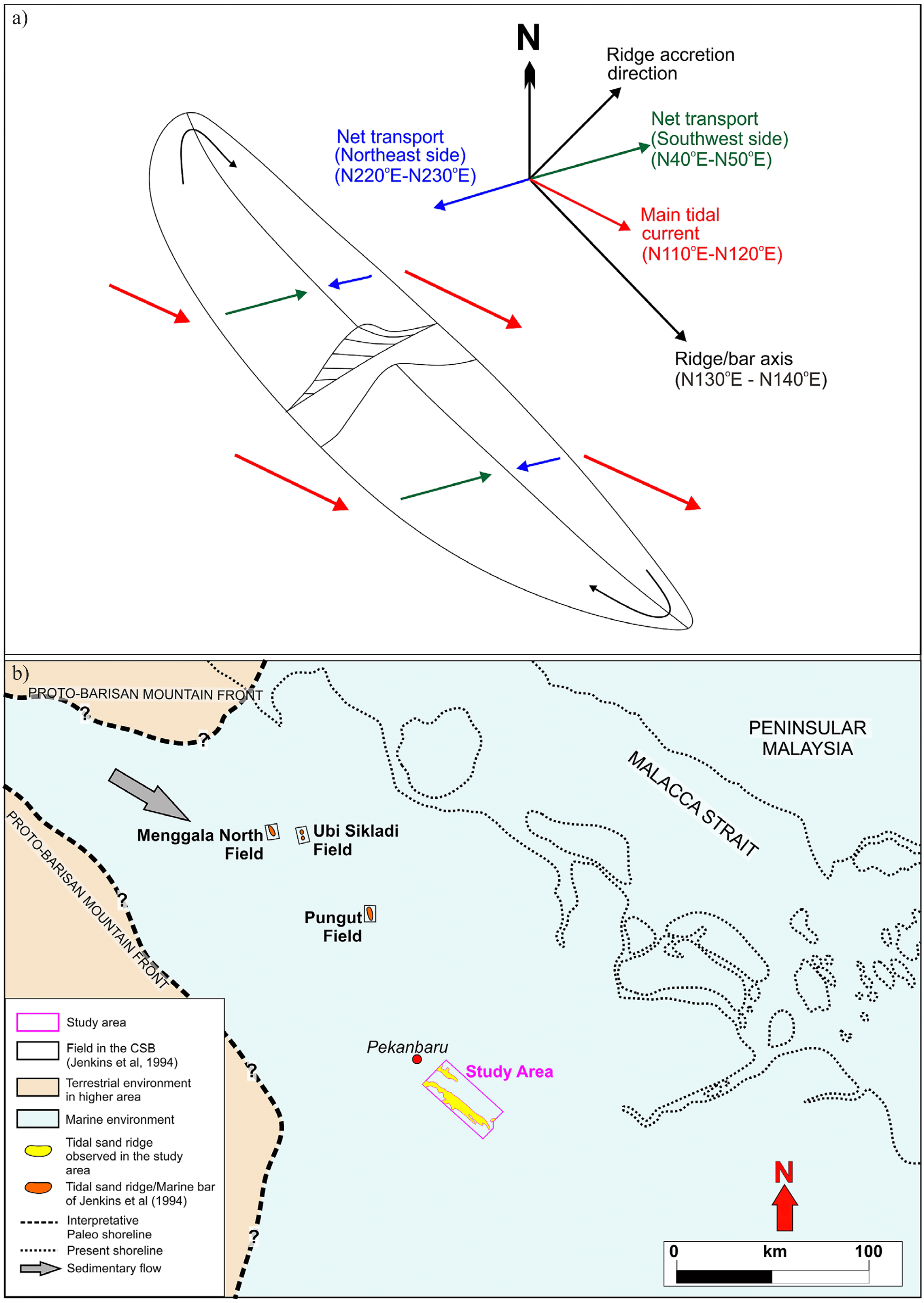

Figure 9: (a) A schematic illustration of a tidal bar, modified from **Reynauld and Dalrymple (2012)** and **Lopez et al. (2016)**. The schematic shows a hypothetical reconstruction of the main tidal current and the resultant net sediment transport in the study area. (b) A sketch of the paleogeographic reconstruction of the CSB during the Middle to Late Miocene. This reconstruction uses information on high amplitude anomalies in the intra-Binio/Petani Formation from this study and Jenkins et al. (1994), illustrating the generally NW-trending orientation of tidal sand ridges. These orientations suggest that the paleo-shoreline was perpendicular or oblique to the ridge orientations during the Middle to Late Miocene. The Proto-Barisan Mountains are speculatively interpreted based on suggestions that it had completely submerged and became a sediment source for the Binio Formation (**Eubank and Makki, 1981; Yarmanto et al., 1995**; **Barber et al., 2005**). The red arrow in **Figure 9b** indicates the North (N) direction.

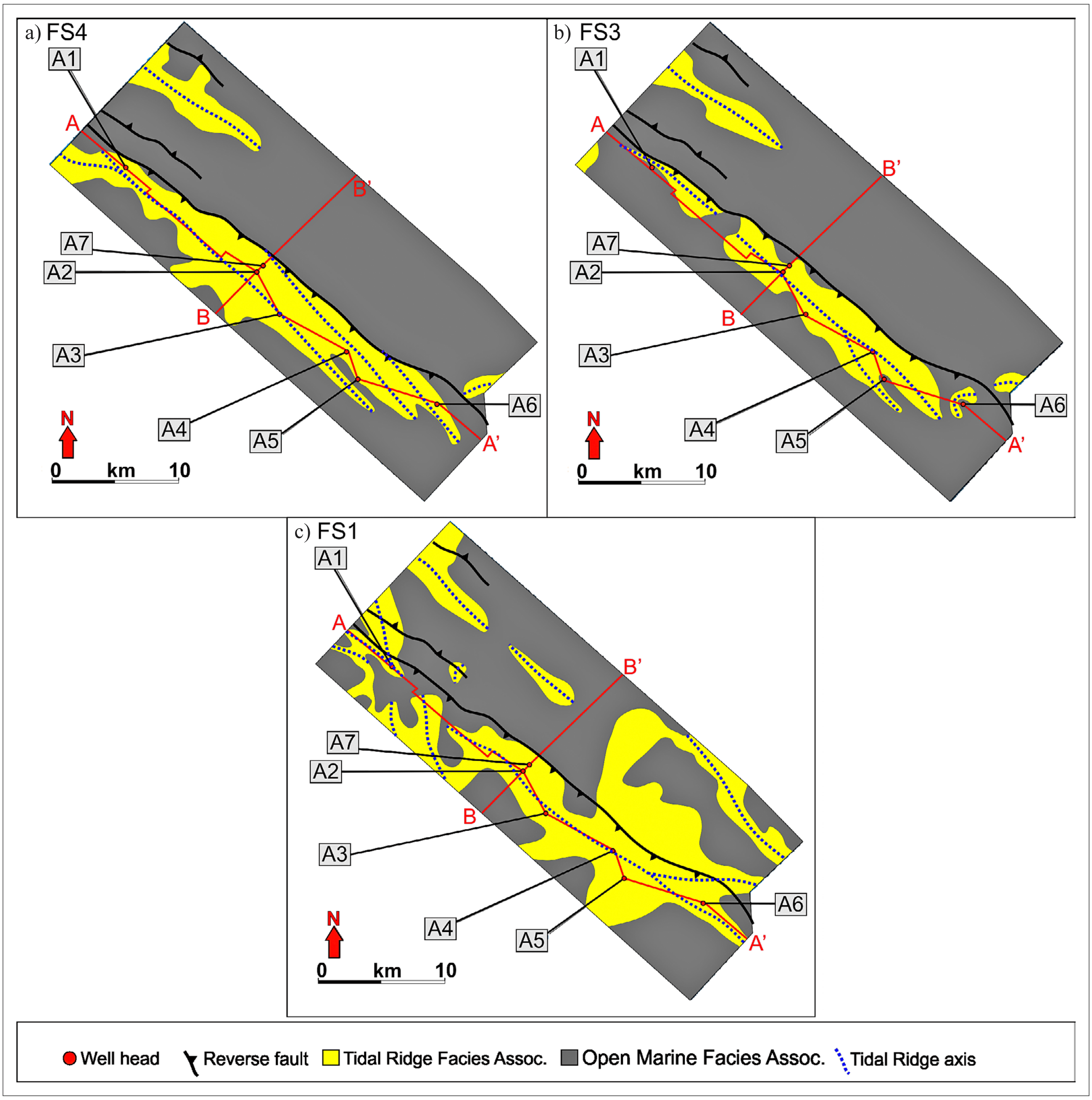

Figure 10: Paleogeographic reconstruction of the Binio Formation deposition in the study area during the time of deposition of (a) FS4, (b) FS3, and (c) FS1. The red arrow indicates the North (N) direction.

ing the deposition of the tidal sand bodies. This interpretation is supported by the observations that: (i) high amplitudes in FS3 and FS4 are generally bounded by the faults (see **Figure 8a-b**); and, (ii) the thickness of the interval between the Binio Formation and FS6 thins on the southwestern flank of a reverse fault, reflecting growth of the reverse fault (F1; **Figure 6b**). This interpretation is similar with the control of faults and/or related fold growth on facies distributions and sediment dispersal, such as the influence of normal faults on the distribution of shoreface and delta-plain facies (**Back et al., 2006**), or the control of thrust faults and related folds on tidal-related facies (**Martinius, 2012**). Second, the NW-trending distribution of the tidal sand bodies may represent their sediment dispersal pattern. This interpretation is supported by: (i) high amplitudes distributed across reverse faults at FS1; (ii) high amplitudes far from the faults with NW-trending orientations, such as those in the northern part of FS4 and FS3 and central part of FS1 (see **Figure 8**). This NW-trending orientation is consistent with high amplitudes within the intra-Binio Formation in Ubi Sikladi Field, which is located far from faults (**Figure 1b; Jenkins et al., 1994**).

It is suggested that the distribution of tidal sand bodies in the study area likely indicates an interplay between sedimentary dispersal, accommodation, and the growth of reverse faults during the Middle-Late Miocene. During the establishment of FS3 and FS4, the distribution of tidal sand bodies was mainly controlled by a combination of sedimentary dispersal and likely the growth of reverse faults. At this time, the reverse faults grew, resulting in limited sedimentary accommodation on the hanging wall of the faults. It is likely that the growth rate of the reverse faults exceeded the rate of sedimentary supply during the establishment of FS3 and FS4, thus limiting the distribution of the tidal sand bodies, which are reflected by high amplitudes, and preventing them from crossing the faults (see **Figure 8a-b**). However, during the establishment of FS1, the distribution of tidal sand bodies was mainly controlled by sedimentary dispersal, with the growth rate of the reverse faults locally influencing their distribution. During this period, the sedimentary supply likely exceeded the growth rate of the reverse faults, surpassing the accommodation space on the hanging wall of the faults and allowing the tidal sand bodies, indicated by high amplitudes, to be distributed across the faults (see **Figure 8c**). The findings regarding the relationship between reverse fault growth and sediment supply in the CSB are considered similar to field observations of tidal deposits in the thrust sheets of the Pyrenees (**Martinius, 2012**). The previous study showed that compressional tectonics could impact the position and relative dimensions of depositional environments, with tidal amplification reducing during thrust sheet growth and leading to narrower zones of shallow water tidalites. Although this study in the CSB cannot determine the water depth indicating tidal amplification during the deposition of tidal-related deposits, it is suggested that the interplay between sedimentary supply rates and accommodation, likely influenced by reverse fault growth rates, played a crucial role in the lateral distribution of the tidal sand bodies. This hypothesis is supported by evidence of uplift in the Barisan Mountain since the Middle Miocene until the Recent, which likely increased sedimentary supply rates in Central Sumatra (e.g. **Mertosono and Nayoan, 1974; Eubank and Makki, 1981; Heidrick and Aulia, 1993**).

The tidal sand bodies, which are interpreted as tidal sand ridges, combined with their distribution at the structural level of FS1 and the high amplitude evidence from **Jenkins et al. (1994)**, suggest the geometry of a paleo-shoreline in Sumatra during the deposition of the Middle-Late Miocene Binio Formation. The NW-trending tidal sand bodies at the FS1 level suggest an axis of the Middle-Late Miocene tidal sand ridges oriented N130°E ± 10° (see **Figure 8**). This orientation is parallel to the high amplitude orientation within the intra-Binio Formation observed by **Jenkins et al. (1994)**, and it infers a tidal current direction of N110°E ± 10°, with net transport directions of N50°E ± 10° and N230°E ± 10° on either side of the tidal sand ridges (c.f. **Reynauld and Dalrymple, 2012; Lopez, 2016**; **Figure 9a**). This NW-SE direction of the inferred tidal current is consistent with the present location of the Barisan Mountain, which lies northwest of the study area (see **Figure 1**). This mountain was a source of sediment for the Central Sumatra Basin (CSB) during the Middle-Late Miocene (e.g. **Eubank and Makki, 1981; Morton et al., 1994; Barber et al., 2005**). These observations indicate that tidal currents might have played a role in transporting sediment from the Barisan Mountain to the CSB during the deposition of the Binio Formation. It is also suggested that the paleo-shoreline in the Middle-Late Miocene was located northwest of the study area and oriented perpendicular to oblique to the ridges (see **Figure 9b**). This inferred orientation of the paleo-shoreline and its association with the tidal sand bodies in the Middle-Late Miocene is consistent with natural examples of tidal sand ridges in estuarine and shallow shelf environments in the East China Sea. These tidal sand ridges in the East China Sea occurred during transgressive and/or regressive system tracts (**Wu et al., 2017**) and are oriented perpendicular to oblique to the shoreline (e.g. **Yang, 1989; Berne et al., 2002; Liu et al., 2007**).

5.3. *Paleogeographic reconstruction*

The spatial distributions of facies associations within the Kiri Trough of the CSB during the Middle-Late Miocene have been highlighted based on the interpretation from conventional core and well correlations. These distributions are clarified through paleogeographic reconstructions representing the early (FS4), middle (FS3), and late (FS1) depositions of the Binio Formation (see **Figure 10**). The paleogeographic reconstruction was derived from the interpretation of core and well correlations, combined with the distribution of high amplitudes in RMS attribute. The RMS attribute indicate that the high amplitudes are consistent with tidal sand body facies (see **Figures 7** and **8**). These high amplitudes are generally laterally enclosed by low amplitudes, indicating tidal sand bodies surrounded by open marine facies. The following section explains the paleogeographic reconstruction up to (i.e. sub) the selected relative time events (i.e. FS1, FS3, and FS4) within the Binio Formation, emphasizing how sediment supply, accommodation space, and sea-level changes influenced the variation of lateral and vertical geometries and facies in the tidal-dominated settings of the Binio Formation.

5.3.1. Sub-FS4

Prior to the development of FS4, marine-dominated deposition of the Telisa Formation prevailed across much of the study area. This is reflected in the widespread presence of the Telisa Formation throughout much of the study area (see **Figures 5-6**). The deposition was associated with a sea-level rise across Southeast Asia, reaching up to SEA59A (**Figure 2; Morley, 2021**), coinciding with the period of maximum transgression in the Middle Miocene (e.g. **De Coster, 1975; Williams and Eubank, 1995; Barber et al., 2005**).

The deposition of the Telisa Formation was followed by the accumulation of tidal sand ridges, formed during the growth of the reverse faults. These tidal sand ridges were deposited during either transgressive or regressive system tracts that continued until the establishment of FS4 (see **Figures 5-6**). These ridges were formed during the transgression through a combination of erosional processes on the shoreface during sea-level rise and tidal reworking, while those formed during the regression resulted from cyclical aggradation and progradation associated with long-term sea-level fall and tectonic uplift. During the FS4 phase, the tidal sand ridges were deposited broadly across the northern, western and southern parts of the study area (A1-A7; **Figures 5-6** and **10c**). However, their lateral extent was constrained by NW-trending reverse faults (see **Figure 10c**), indicating that the growth rate of the reverse faults likely exceeded sedimentary supply during the FS4 phase.

5.3.2. Sub-FS3

Following the FS4 phase and prior to the formation of FS3, the study area experienced flooding, leading to widespread deposition of open marine facies (see **Figures 5** and **6**). This deposition phase was associated with the rise of a flooding surface, which reached its maximum at MFS4. Although the maximum flooding surface at MFS4 has not been documented in other parts of the CSB, evidence of small-scale sea-level fluctuations in Southeast Asia during the deposition of the Binio Formation has been suggested, ranging from SEA59A to SEA61 (**Morley et al., 2021**; **Figure 2**). These regional sea-level changes may reflect conditions associated with the maximum transgression at MFS4.

During the FS3 phase, tidal sand ridges, represented by tidal sand bodies, were locally deposited across the study area (see **Figure 10b**). These ridges, formed near FS3, displayed a narrower lateral extent compared to those observed near FS4 (see **Figure 10b**), suggesting a reduction in sedimentary supply during the FS3 phase relative to FS4. This reduction may be associated with interruptions and renewal of sedimentation in the Binio Formation, as recorded at the margin of the CSB (**De Coster, 1975**). As in FS4, the distribution of the tidal sand ridges in the central part of the study area was constrained by reverse faults (see **Figure 10b**), indicating that the growth rate of these inversion faults continued to exceed the sedimentary supply during the FS3 phase.

5.3.3. Sub-FS1

Following the FS3 phase and before the formation of the maximum flooding surface at MFS2, tidal sand ridges were variably distributed across the study area. These ridges were locally deposited in the northwest (A1-A2), central (A4), and southeast (A6) during the development of the maximum flooding surface at MFS3 (see **Figure 5a**). This phase was followed by thickening and a gradual lateral expansion of the ridges during establishment of FS2 (A1-A6**; Figure 5**). However, during the formation of the maximum flooding surface at MFS2, the thickness and lateral extent of these ridges decreased. Similar to their development during FS4, the formation of these ridges can be attributed to transgressive and regressive system tracts.

From the MFS2 phase until the FS1 phase, the distribution of tidal sand ridges varied both vertically and laterally across the study area (see **Figures 5-6**). During this time, the tidal sand ridges likely extended across inversion faults (see **Figure 10a**), indicating that the sedimentary supply surpassed the growth rate of these inversion faults. This increase sedimentary supply may be linked to the uplift of the Barisan Mountain during the Middle-Late Miocene (**Figure 2**; e.g. **Mertosono and Nayoan, 1974; Eubank and Makki, 1981; Heidrick and Aulia, 1993**), a tectonic event that likely contributed to a higher sediment influx into the study area.

6. Conclusions

Facies and sequence stratigraphic analyses were conducted on core and wireline logs, along with horizon mapping in 3D seismic data, to understand the variability and distribution of facies in the Binio Formation, which was deposited in the Kiri Trough during the Middle-Late Miocene basin inversion. The analysis revealed that the formation consists of tidal sand bodies and open marine facies. Through GR log profiles and mud log data, six flooding and four maximum flooding surfaces were defined, which allowed the construction of a sequence stratigraphic framework. This framework indicated that tidal sand bodies formed during or after the establishment of maximum flooding surfaces, reflecting transgressive and regressive tidal sand ridges, respectively. Horizon mapping of flooding surfaces in the RMS attribute highlighted the lateral geometry of the ridges and their relationship with reverse faults. The consistent NW-trending orientation of these ridges in the attribute implies a NW-trending tidal current that facilitated sediment transport from a paleo-shoreline located perpendicular to oblique to the ridges, near the Barisan Mountain during the Middle-Late Miocene. Furthermore, this study illustrated, for the first time, that the growth of reverse faults during the Middle-Late Miocene likely controlled the distribution of tidal sand bodies in the Binio Formation within the CSB. The study identified tidal sand ridge distributions, confined by reverse faults during the early-middle deposition and extending across the faults in the final phase of Binio Formation deposition. This temporal and spatial evolution reflects the interaction between sediment supplies, and accommodation spaces, influenced by reverse fault growth and sea-level variations. These findings provide insight into facies variations and distributions around growth structures, such as those observed in other inverted back-arc basins in Sumatra, Indonesia, or foreland basin like the Pyrenees. The distribution of these ridges also suggests the possible existence of a NE-trending paleo-shoreline during the Middle to Late Miocene.

Acknowledgement

We thank the management of Energi Mega Persada Bentu Limited (EMP Bentu Ltd), Dirjen Migas and SKK Migas for their permission to publish this study. We also wish to thanks for all effort and cooperation to all staff in Energi Mega Persada Bentu Limited. The authors also acknowledge Rock Flow Dynamics for the provision of a license for Geological Designer in tNavigator software to this study.

7. References

Allen, J. R. (1982): Sedimentary Structures Their Character and Physical Basis (Vol. 1). Elsevier Scientific Publishing Company, Amsterdam.

Ashraf, U., Zhu, P., Yasin, Q., Anees, A., Imraz, M., Mangi, H. N., & Shakeel, S. (2019): Classification of reservoir facies using well log and 3D seismic attributes for prospect evaluation and field development: A case study of Sawan gas field, Pakistan. Journal of Petroleum Science and Engineering, 175, 338-351. https://doi.org/10.1016/j.petrol.2018.12.060

Azeem, T., Yanchun, W., Khalid, P., Xueqing, L., Yuan, F., & Lifang, C. (2016): An application of seismic attributes analysis for mapping of gas bearing sand zones in the sawan gas field, Pakistan. Acta Geodaetica et Geophysica, *51*(4), 723-744. https://doi.org/10.1007/s40328-015-0155-z

Back, S., Höcker, C., Brundiers, M. B., & Kukla, P. A. (2006): Three-dimensional-seismic coherency signature of Niger Delta growth faults: integrating sedimentology and tectonics. Basin Research, 18(3), 323-337. https://doi.org/10.1111/j.1365-2117.2006.00299.x

Barber, A. J., Crow, M. J., & Milsom, J. S. (2005): Sumatra: Geology, Resources and Tectonic Evolution (Vol. 31). Geological Society, London.

Berné, S., Vagner, P., Guichard, F., Lericolais, G., Liu, Z., Trentesaux, A., Yin, P., & Yi, H. I. (2002): Pleistocene forced regressions and tidal sand ridges in the East China Sea. Marine Geology, 188(3), 293-315. https://doi.org/10.1016/S0025-3227(02)00446-2

Berne, S., Lericolais, G., Marsset, T., Bourillet, J. F., & De Batist, M. (1998): Erosional offshore sand ridges and lowstand shorefaces; examples from tide- and wave-dominated environments of France. Journal of Sedimentary Research, 68(4), 540-555. https://doi.org/10.2110/jsr.68.540

Blatt, H., Middleton, G. V., & Murray, R. C. (1980): Origin of Sedimentary Rocks. Prentice-Hall, New Jersey.

Boggs, S. (2014): Principles of Sedimentology and Stratigraphy. Pearson Education Limited, Essex.

Bruun, P. (1962): Sea-Level Rise as a Cause of Shore Erosion. Journal of the Waterways and Harbors Division, 88(1), 117-130. https://doi.org/10.1061/JWHEAU.0000252

Cannon, S. (2016): Petrophysic: A practical Guide. Wiley Blackwell. https://doi.org/10.1002/9781119117636

Catuneanu, O. (2006): Principles of Sequence Stratigraphy. Elsevier, Amsterdam.

Catuneanu, O., Galloway, W. E., Kendall, C., Miall, A. D., Posamentier, H. W., Strasser, A., & Tucker, M. E. (2011): Sequence Stratigraphy: Methodology and Nomenclature. Newsletters on Stratigraphy, 44(3), 173-245. https://doi.org/10.1127/0078?0421/2011/0011

Cooper, M., & Warren, M. J. (2020): Inverted fault systems and inversion tectonic settings. In: N. Scarselli, J. Adam, D. Chiarella, D. G. Roberts, & A. W. Bally (Eds.): Regional Geology and Tectonics (Second Edition*)*. Elsevier., pp. 169-204. https://doi.org/10.1016/B978-0-444-64134-2.00009-2

Dalrymple, R. W., Knight, R. J., Zaitlin, B. A., & Middleton, G. V. (1990): Dynamics and facies model of a macrotidal sandbar complex, Cobequid Bay – Salmon River Estuary (Bay of Fundy). Sedimentology, 37(4), 577-612. https://doi.org/https://doi.org/10.1111/j.1365-3091.1990.tb00624.x

De Coster, G. L. (1974): The geology of the Central and South Sumatra basins. Indonesian Petroleum Association 3rd Annual Convention & Exhibition, Jakarta.

Dominguez, J. M. L., & Wanless, H. R. (1992): Facies Architecture of a Falling Sea-Level Strandplain, Doce River Coast, Brazil. In *Shelf Sand and Sandstone Bodies* (pp. 257-281). https://doi.org/10.1002/9781444303933.ch7

Eubank, R. T., & Makki, A. C. (1981): Structural Geology of the Central Sumatra Back-Arc Basin. Indonesian Petroleum Association 10th Annual Convention & Exhibition, Jakarta.

Fakhruddin, R., Sunardi, E., Gumelar Adhiperdana, B., Heri Hermiyanto Zajuli, M., Ramli, T., Mersil Saleh, H., Perdana Putra, A., Sabra, E., & Ghia Arvyalin, G. (2023): Late Miocene to Pliocene delta-lacustrine to incised-valley fills sedimentation of the Ransiki Area, Bird's Head Papua, Indonesia: The sedimentary record of Lengguru Fold and Thrust Belt wedge-top depozone. Journal of Asian Earth Sciences, 242, 105497. https://doi.org/10.1016/j.jseaes.2022.105497

Galloway, W. E. (1989): Genetic Stratigraphic Sequences in Basin Analysis I: Architecture and Genesis of Flooding-Surface Bounded Depositional Units. AAPG Bulletin, 73(2), 125-142. https://doi.org/10.1306/703C9AF5-1707-11D7-8645000102C1865D

Gebco Compilation Group (2020): The GEBCO_2020 Grid - a continuous terrain model of the global oceans and land, British Oceanographic Data Centre, National Oceanography Centre. https://www.bodc.ac.uk/

Geoservices. (2019): Routine & Special Core Analysis, Rock Description & Biostratigraphy For Conventional Core & Ditch Cutting Samples From Well Seng-04 (2019/0817/LAB) [Unpublished Report]. Energi Mega Persada Bentu Limited.

Ginger, D. C., Ardjakusumah, Hedley, R. J., & Pothecary, J. (1993): Inversion history of the West Natuna Basin: examples from the Cumi-Cumi PSC. Indonesian Petroleum Association 22nd Annual Convention & Exhibition, Jakarta.

Hedgpeth, J. W. (1957): Chapter 2: Classification of Marine Environments. In: J. W. Hedgpeth (Ed.): Treatise on Marine Ecology and Paleoecology. Geological Society of America. https://doi.org/10.1130/MEM67V1-p17

Heidrick, T. L., & Aulia, K. (1993): A structural and tectonic model of the Coastal Plains Block, Central Sumatra Basin, Indonesia. Indonesian Petroleum Association 22nd Annual Convention & Exhibition, Jakarta.

Jenkins, S. D., Hendar, S. M., & Kodl, E. J. (1994): Integrated analysis of Petani gas sands in selected fields Central Sumatra. Indonesian Petroleum Association 23rd Annual Convention, Jakarta.

Kieft, R. L., Jackson, C. A. L., Hampson, G. J., & Larsen, E. (2010): Sedimentology and sequence stratigraphy of the Hugin Formation, Quadrant 15, Norwegian sector, South Viking Graben. Geological Society, London, Petroleum Geology Conference Series, 7(1), 157-176. https://doi.org/10.1144/0070157

Lee, R. A. (1982): Petroleum Geology Of The Malacca Strait Contract Area (Central Sumatra Basin). Indonesian Petroleum Association 11th Annual Convention, Jakarta.

Liu, Z., Yin, P., Xiong, Y., Berne, S., Trentesaux, A., & Li, C. (2007): Quaternary transgressive and regressive depositional sequences in the East China Sea. Chinese Science Bulletin, 48(1), 81-87. https://doi.org/10.1007/BF02900944

Longhitano, S. G., Rossi, V. M., Chiarella, D., Mellere, D., Tropeano, M., Dalrymple, R. W., Steel, R. J., Nappi, A., & Olita, F. (2021): Anatomy of a mixed bioclastic–siliciclastic regressive tidal sand ridge: Facies-based case study from the lower Pleistocene Siderno Strait, southern Italy. Sedimentology, 68(6), 2293-2333. https://doi.org/https://doi.org/10.1111/sed.12853

López, J. L., Rossi, V. M., Olariu, C., & Steel, R. J. (2016): Architecture and recognition criteria of ancient shelf ridges; an example from Campanian Almond Formation in Hanna Basin, USA. Sedimentology, 63(6), 1651-1676. https://doi.org/https://doi.org/10.1111/sed.12279

Loutit, T. S., Hardenbol, J., Vail, P. R., & Baum, G. R. (1988): Condensed Sections: The Key to Age Determination and Correlation of Continental Margin Sequences. In: C. K. Wilgus, B. S. Hastings, H. Posamentier, J. V. Wagoner, C. A. Ross, & C. G. S. C. Kendall (Eds.): Sea-Level Changes: An Integrated Approach (Vol. 42). SEPM Society for Sedimentary Geology. https://doi.org/10.2110/pec.88.01.0183

Martinius, A. W. (2012): Contrasting Styles of Siliciclastic Tidal Deposits in a Developing Thrust-Sheet-Top Basins – The Lower Eocene of the Central Pyrenees (Spain). In: R. A. Davis Jr & R. W. Dalrymple (Eds.), Principles of Tidal Sedimentology. Springer Netherlands, pp. 473-506. https://doi.org/10.1007/978-94-007-0123-6_18

Mertosono, S. (1975): Geology of Pungut and Tandun oil fields, Central Sumatra. Indonesian Petroleum Association 4th Annual Convention.

Mertosono, S., & Nayoan, G. A. S. (1974): The Tertiary basinal area of Central Sumatra. Indonesian Petroleum Association 3rd Annual Convention.

Morley, R. J., Hasan, S. S., Morley, H. P., Jais, J. H. M., Mansor, A., Aripin, M. R., Nordin, M. H., & Rohaizar, M. H. (2021): Sequence biostratigraphic framework for the Oligocene to Pliocene of Malaysia: High-frequency depositional cycles driven by polar glaciation. Palaeogeography, Palaeoclimatology, Palaeoecology, 561. https://doi.org/10.1016/j.palaeo.2020.110058

Morley, R. J., Morley, H. P., & Swiecicki, T. (2016): Mio-Pliocene Palaeogeography, Uplands And River Systems of the Sunda Region Based on Mapping Within a Framework of Vim Depositional Cycles. Indonesian Petroleum Association 40th Annual Convention.

Morton, A. C., Humphreys, B., Dharmayanti, D. A., & Sundoro. (1994): Palaeogeographic implications of the heavy mineral distribution in Miocene sandstones of the North Sumatra Basin. Journal of Southeast Asian Earth Sciences, 10(3), 177-190. https://doi.org/https://doi.org/10.1016/0743-9547(94)90018-3

Olariu, C., Steel, R. J., Olariu, M. I., & Choi, K. (2015): Facies and architecture of unusual fluvial–tidal channels with inclined heterolithic strata: Campanian Neslen Formation, Utah, USA. In: P. J. Ashworth, J. L. Best, & D. R. Parsons (Eds.): Developments in Sedimentology, pp. 353-394. Elsevier. https://doi.org/10.1016/B978-0-444-63529-7.00011-0

Plink-BjÖRklund, P. (2005): Stacked fluvial and tide-dominated estuarine deposits in high-frequency (fourth-order) sequences of the Eocene Central Basin, Spitsbergen. Sedimentology, 52(2), 391-428. https://doi.org/10.1111/j.1365-3091.2005.00703.x

Posamentier, H. W. (2002): Ancient Shelf Ridges – A Potentially Significant Component of the Transgressive Systems Tract: Case Study from Offshore Northwest Java. AAPG Bulletin, 86(1), 75-106. https://doi.org/10.1306/61EEDA44-173E-11D7-8645000102C1865D

Posamentier, H. W., & Allen, G. P. (1999): Siliciclastic Sequence Stratigraphy – Concepts and Applications. SEPM Society for Sedimentary Geology. https://doi.org/10.2110/csp.99.07

Posamentier, H. W., & Vail, P. R. (1988): Eustatic Controls on Clastic Deposition II – Sequence and Systems Tract Models. In Sea-Level Changes: An Integrated Approach (Vol. 42). Society of Economic Paleontologists and Mineralogists. https://doi.org/10.2110/pec.88.01.0125

Pubellier, M., & Morley, C. K. (2014): The basins of Sundaland (SE Asia): Evolution and boundary conditions. Marine and Petroleum Geology, 58, 555-578. https://doi.org/10.1016/j.marpetgeo.2013.11.019

Ramli, M. N. (1988): Stratigraphy and Palaeofacies Development of Carigali's Operating Areas in the Malay Basin, South China Sea. Bulletin of the Geological Society of Malaysia, 22, 153-187. https://doi.org/10.7186/bgsm22198808

Reynaud, J.-Y., & Dalrymple, R. W. (2012): Shallow-Marine Tidal Deposits. In: R. A. Davis Jr & R. W. Dalrymple (Eds.): Principles of Tidal Sedimentology. 335-369. Springer Netherlands. https://doi.org/10.1007/978-94-007-0123-6_13

Roberts A. M., Price John, D., & Olsen Terkel, S. (1990): Late Jurassic half-graben control on the siting and structure of hydrocarbon accumulations: UK/Norwegian Central

Graben. Geological Society, London, Special Publications, 55(1), 229-257. https://doi.org/10.1144/GSL.SP.1990.055.01.11

Roezin, S. (1974): The discovery and development of the Petapahan oil field, Central Sumatra. Indonesian Petroleum Association 3rd Annual Convention, Jakarta.

Setiawan, A., Siregar, R., Arief, D., Rakimi, S., Sodli, A., Wisnu Y., R., & Hendarman. (2014): Integration of Seismic Attributte and Sedimentation Concept for Paleogeographic and Sand Distribution Modeling in Seng-Segat Field, Bentu Block, Central Sumatra Basin. Indonesian Petroleum Association 38th Annual Convention & Exhibition, Jakarta.

Shanley, K. W., McCabe, P. J., & Hettinger, R. D. (1992): Tidal influence in Cretaceous fluvial strata from Utah, USA: a key to sequence stratigraphic interpretation. Sedimentology, 39(5), 905-930. https://doi.org/10.1111/j.1365-3091.1992.tb02159.x

Sundararaman, P., & Teerman, S. C. (1991): Porphyrins in extracts as indicators of maturity and depositional environment of tertiary source rocks from Central Sumatra. Indonesian Petroleum Association 20th Annual Convention, Jakarta.

Wagoner, J. C. V., Mitchum, R. M., Campion, K. M., & Rahmanian, V. D. (1990): Siliciclastic Sequence Stratigraphy in Well Logs, Cores, and Outcrops: Concepts for High-Resolution Correlation of Time and Facies. American Association of Petroleum Geologists. https://doi.org/10.1306/Mth7510

Williams Harold, H., & Eubank Roger, T. (1995): Hydrocarbon habitat in the rift graben of the Central Sumatra Basin, Indonesia. Geological Society, London, Special Publications, 80(1), 331-371. https://doi.org/10.1144/GSL.SP.1995.080.01.16

Wongsosantiko, A. (1976): Lower Miocene Duri Formation sands, Central Sumatra Basin. Proceedings Indonesian Petroleum Association 5th Annual Convention, Jakarta.

Yakzan, A. M., Harun, A., Md Nasib, B., & Morley, R. J. (1996): Integrated biostratigraphic zonation for the Malay Basin. Bulletin of the Geological Society of Malaysia, 39, 157-184. https://doi.org/10.7186/bgsm39199615

Yang, C.-S. (1989): Active, moribund and buried tidal sand ridges in the East China Sea and the Southern Yellow Sea. Marine Geology, 88(1), 97-116. https://doi.org/https://doi.org/10.1016/0025-3227(89)90007-8

Yarmanto, Heidrick, T. L., Indrawardana, & Strong, B. L. (1995): Tertiary tectonostratigraphic development of the Balam depocenter, Central Sumatra basin, Indonesia. Indonesian Petroleum Association 24th Annual Convention, Jakarta.

Yuwono, R. W., Fitriana, B. S., Kirana, P. S., Djaelani, S., & Sjafwan, B. A. (2012): Biogenic Gas Exploration and Development in Bentu PSC, Central Sumatra Basin, Indonesia. AAPG International Conference and Exhibition, Singapore.

Zhang, X., Ding, L., Du, J., Liu, D., & Liu, H. (2017): Sedimentary characteristics and controlling factors of shelf sand ridges in the Pearl River Mouth Basin, northeast of South China Sea. Journal of Natural Gas Geoscience, 2(2), 141-155. https://doi.org/10.1016/j.jnggs.2017.04.001

Zhuo, H., Wang, Y., Shi, H., Zhu, M., He, M., Chen, W., & Li, H. (2014): Seismic geomorphology, architecture and genesis of Miocene shelf sand ridges in the Pearl River Mouth Basin, northern South China Sea. Marine and Petroleum Geology, 54, 106-122. https://doi.org/10.1016/j.marpetgeo.2014.03.002

SAŽETAK

Plimne naslage srednjomiocenske do gornjomiocenske formacije Binio: sedimentni i stratigrafski zapisi tijekom inverzije bazena središnje Sumatre, Indonezija

Raspored plimnih naslaga može biti upravljan strukturnim rastom koji se odražava, primjerice, u pojavi inverznih struktura u zalučnom bazenu. Primjer takve strukture nalazi se u bazenu središnje Sumatre (CSB), Indonezija. Međutim, do sada su postojala samo ograničena detaljna istraživanja koja su upotrebljavala 3D seizmičke podatke te podatke o bušotinama i jezgri radi razumijevanja načina kako strukturni rast upravlja taložnim procesima i rasporedom plimnih naslaga u CSB-u. U ovome istraživanju korištene su navedene vrste podataka u svrhu proučavanja taložnih procesa te rasporeda naslaga srednjomiocenske do gornjomiocenske formacije Binio koja je nastala tijekom tektonske inverzije navedenoga bazena. Na tim je podatcima provedena sedimentološka analiza, sekvencijska stratigrafija i analiza atributa kvadratnoga korijena srednje vrijednosti (RMS). Sedimentološka analiza jezgre otkrila je prisutnost plimnoga pješčanog tijela i facijesa otvorenoga mora. Nadalje, integracijom karotaže prirodne radioaktivnosti i rezultata laboratorijskih analiza identificirane su serije parasekvencija ograničene površinama preplavljivanja. Unutar toga stratigrafskog okvira pješčana tijela pojavljivala su se prije i nakon površina maksimalnoga preplavljivanja tvoreći transgresivne i regresivne plimne pješčane prudove. Analiza RMS atributa u blizini tih površina pokazala je dosljednu orijentaciju ovih prudova u smjeru sjeverozapada, što upućuje na utjecaj plimnih struja u smjeru sjeverozapada, kao i paleoobale usmjerene prema sjeverozapadu u blizini planine Barisan, a što je utjecalo na raspored sedimenata te paleogeografiju tijekom srednjega i kasnoga miocena. Dodatno, istraživanje odnosa između prudova i reversnih rasjeda otkrilo je da su prudovi vjerojatno upravljani tektonskom aktivnošću. Ovim istraživanjem naglašeno je da je vremenski i prostorni razvoj prudova u CSB-u bio vođen interakcijom donosa sedimenta i smještajnoga prostora, koja je vjerojatno bila pod utjecajem rasta reverznoga rasjeda i promjena razine mora.

Ključne riječi:
formacija Binio, plimni pješčani prud, inverzija bazena, bazen središnje Sumatre, sekvencijska stratigrafija

Author’s contribution

Aurio Erdi (Phd, Senior Geoscientist, Structural Geology and Tectonic) as a main contributor, performing seismic interpretation and attribute analysis, sequence stratigraphy, well correlation and presentation of the results. **Afrizon Setiawan** (M. Sc, Senior Geologist, Geology) as an advisor, providing feedback on seismic interpretation, petrophysics, well correlations and geological conceptual models. **Ismail Zulmi** (B. Sc, Senior Geologist, Geology) as an advisor, providing feedback on seismic interpretation, petrophysics, well correlations and geological conceptual models. **Alan Rene Inabuy** (M. Sc. Senior Geophysicist, Geophysicist) as an advisor, providing feedback on seismic interpretation and attributes. **Rifati Hanifa Az Zahra** (B. Sc, Geologist, Geology) as an advisor, providing feedback on seismic interpretation, petrophysics, well correlations and geological conceptual models. **Eric Edwin** (B. Sc, Geologist, Geology) as an advisor, providing feedback on seismic interpretation, petrophysics, well correlations and geological conceptual models. **Ivan Praja Andhika** (M. Sc, Senior Geoscientist, Geology) as a supporting contributor, providing feedback on seismic interpretation, petrophysics, well correlations and geological conceptual models

Dany Auliansyah (M. Sc, Senior Petrophysics, Geology and Petrophysics) as a supporting contributor, performing petrophysics analysis. **Edward Wijaya** (B. Sc, Junior Geologist, Geology) as a supporting contributor, performing seismic interpretations.